Simulating the mass balance and salinity of Arctic and Antarctic sea ice. 1. Model description and validation

Martin Vancoppenolle [a,*], Thierry Fichefet [a], Hugues Goosse [a], Sylvain Bouillon [a], Gurvan Madec [b,c], Miguel Angel Morales Maqueda [d]

[a] Institut d'Astronomie et de Géophysique Georges Lemaître, Université catholique de Louvain, Bâtiment Marc de Hemptinne, Chemin du cyclotron, 2, 1348 Louvain-la-Neuve, Belgium
[b] Laboratoire d'Océanographie et du Climat (LOCEAN), Paris, France
[c] National Oceanographic Centre, Southampton, UK
[d] Proudman Oceanographic Laboratory, Liverpool, UK

ARTICLE INFO

ABSTRACT

This paper is the first part of a twofold contribution dedicated to the new version of the Louvain-la-Neuve sea ice model LIM3. In this part, LIM3 is described and its results are compared with observations. LIM3 is a C-grid dynamic–thermodynamic model, including the representation of the subgrid-scale distributions of ice thickness, enthalpy, salinity and age. Brine entrapment and drainage as well as brine impact on ice thermodynamics are explicitly included. LIM3 is embedded into the ocean modelling system NEMO, using OPA9, a hydrostatic, primitive equation, finite difference ocean model in the $2° \times 2°cos\phi$ configuration ORCA2. Model performance is evaluated by performing a hindcast of the Arctic and Antarctic sea ice packs, forced by a combination of daily NCEP/NCAR reanalysis data and various climatologies. The annual cycle of sea ice growth and decay is very realistically captured with ice area, thickness, drift and snow depth in good agreement with observations. In the Arctic, the simulated geographical distributions of ice thickness and concentration are significantly improved when compared with earlier versions of LIM. Model deficiencies feature an overestimation (underestimation) of ice thickness in the Beaufort gyre (around the North Pole) as well as an underestimation of ice thickness in the Southern Ocean. The simulated first year/multiyear sea ice limit agrees with observations. The values and distribution of sea ice age in the perennial ice zone are different from satellite-derived values, which is attributed to the different definitions of ice age. In conclusion, in light of the exhaustive sea ice analysis presented here, LIM3 is found to be an appropriate tool for large-scale sea ice and climate simulations.

© 2008 Elsevier Ltd. All rights reserved.

1. Introduction

Sea ice is a major component of the climate system (e.g., Serreze et al., 2007). It acts as an insulating layer, damping exchanges between atmosphere and ocean. Transfer of radiation, through high albedo (e.g., Perovich et al., 2002; Brandt et al., 2005), of sensible heat, through low thermal conductivity (e.g., Pringle et al., 2007) and of momentum are affected. In addition, the release of salt and freshwater associated with the growth and melt of sea ice (e.g., Widell et al., 2006; Vancoppenolle et al., 2006) have a significant impact on the oceanic stratification and hence on the World Ocean thermohaline circulation (e.g., Aagaard and Carmack, 1989; Goosse and Fichefet, 1999). Sea ice is also a habitat for a group of bacteria and microscopic plants encased in the ice matrix (e.g.,

Ackley and Sullivan, 1994). It carries considerable amounts of iron (Lannuzel et al., 2007) and modulates the polar CO_2 exchanges (e.g., Delille, 2006) through the intermittently open brine network, as well as through leads and polynyas. This places sea ice as an important actor of the polar and global carbon cycles. Finally, sea ice is, on the one hand, sensitive to small external perturbations but also, on the other hand, associated with a series of important feedbacks (e.g., Ebert and Curry, 1993). Therefore, sea ice acts not only as an early indicator of climate change but also as an amplifier of climatic perturbations.

In this context, the changes that were recently observed in the Northern Hemisphere sea ice cover have to be considered with the greatest attention. Passive microwave (PMW) records consistently show that the annual mean Arctic sea ice extent has been decreasing since 1979 by around 3% per decade (Cavalieri et al., 2003), the trend being higher in summer (−9.1% per decade for 1979–2006, see Stroeve et al., 2007). Recently, the retreat accelerated and was characterized by a series of minima of extent (Stroeve et al., 2005; Comiso et al., 2008), with a spectacular historical minimum

* Corresponding author. Tel.: +32 10473064; fax: +32 10474722.
E-mail address: vancop@astr.ucl.ac.be (M. Vancoppenolle).
URL: http://www.astr.ucl.ac.be/index.php?page=vancop%23HomePage (M. Vancoppenolle).

in 2007. A downward winter trend is also observed for a few years, reaching −2.9% per decade (Comiso, 2006). Less is known about ice thickness and volume since observations are sparse. Several recent publications were dedicated to the topic, though. First, a recently updated ice thickness data set from upward-looking sonars (ULS) onboard submarines, including 37 cruises (Rothrock et al., 2003), suggests that Arctic annual mean ice thickness decreased by 1.25 m between 1980 and 2000. Second, the first satellite observations of ice thickness data have been published recently. They give results in agreement with ULS (Laxon et al., 2003; Kwok and Cunningham, 2008; Zwally et al., 2008), but uncertainties are significant, spatial coverage is limited and the length of the time series is too short to derive trends.

Given the magnitude of the recent changes and their potential impact through feedbacks, it is clear that understanding the mechanisms responsible for long-term changes and performing reliable projections are crucial issues of current climate studies. Large-scale sea ice models developed in the last decades (e.g., Fichefet and Morales Maqueda, 1997; Bitz et al., 2001; Zhang and Rothrock, 2003; Hunke and Lipscomb, 2004) are included in the coupled models used to perform climate change projections (see, e.g., Arzel et al., 2006; Zhang and Walsh, 2006). Those models are based on the same dynamic–thermodynamic structure, discretized using finite differences on structured grids. Typically, the model thermodynamic component is based on the Semtner (1976) 0- or 3-layer models, or on the more sophisticated model of Bitz and Lipscomb (1999). The dynamic component solves the ice momentum equation assuming that sea ice behaves as a two-dimensional continuum with a viscous–plastic (VP) rheology, using either the original VP numerical method (Hibler, 1979), the elastic–viscous–plastic (EVP) method (Hunke and Dukowicz, 1997) or a semi-implicit alternate method (Zhang and Hibler, 1997). In addition, some models include the ice thickness distribution (ITD) physics (Thorndike et al., 1975) with various physical (Flato and Hibler, 1995; Zhang and Rothrock, 2003) and numerical (Lipscomb, 2001) improvements. An interactive ITD enables to simulate the faster growth and decay of thin ice (Maykut, 1986), which in turn leads to a more realistic ice-albedo feedback (Holland et al., 2006). Nevertheless, the large uncertainties remaining in, on the one hand, coupled ice–ocean hindcast simulations of the 20th century (e.g., Gerdes and Köberle, 2007), and in IPCC[1] simulations for the 20th and 21st centuries (e.g., Arzel et al., 2006; Lefebvre and Goosse, 2008), on the other hand, stress the need for further model development.

One of the shortcomings of present sea ice models is that they all neglect or misrepresent the sea ice salinity, though significant variations in sea ice salinity have been reported about 80 years ago, with potentially important consequences on ice thermodynamics (Malmgren, 1927). The salt cannot lock into the sea ice crystalline lattice, but is rather dissolved into liquid inclusions of brine. Due to brine entrapment and drainage, the ice salinity varies in space and time (Untersteiner, 1968). Salinity, in association with temperature, controls the relative brine volume encased in the ice, which in turn affects all ice properties (thermal, mechanical and radiative). Recently, a 1-D energy-conserving halo-thermodynamic model (i.e., including a prognostic salinity profile) was developed and tested against observations (Vancoppenolle et al., 2007, hereafter referred to as VBF07). The brine impact on the ice thermal properties influences the seasonal cycle of ice thickness, which in turn affects the exchanges of salt and freshwater between ice and ocean (Vancoppenolle et al., 2006). Therefore, including salinity in global sea ice models is potentially important.

Table 1
List of model parameters and constants.

M	Number of ice categories	5	–
N	Number of vertical ice layers	5	–
C_a	Atmospheric drag coefficient	1.4×10^{-3}	–
C_w	Ice–ocean drag coefficient	5.0×10^{-3}	–
P^*	Ice strength	40,000	Nm^{-1}
C_s	Fraction of energy dissipated by shear	0.5	–
T_e	Elastic wave time scale	9600	s
e^*	Elliptical yield curve eccentricity	2	–
a^*	e-folding participating area coefficient	0.05	–
H^*	Maximum ridged ice thickness coefficient	100	m
h_P	Maximum rafting ice thickness	0.75	m
C_{ra}	Ridging–rafting transition coefficient	5	m^{-1}
p	Initial ridge porosity	0.3	–
ρ_s	Snow density	330	$kg\ m^{-3}$
ρ_i	Sea ice density	917	$kg\ m^{-3}$
ρ_w	Reference seawater density	1020	$kg\ m^{-3}$
k_s	Snow thermal conductivity	0.31	$W\ m^{-1}\ K{-1}$
k_0	Pure ice thermal conductivity	2.01	$W\ m^{-1}\ K{-1}$
c_0	Pure ice specific heat	2067	$J\ kg^{-1}\ K^{-1}$
L_0	Pure ice latent heat of fusion	334×10^3	$J\ kg^{-1}$
L_s	Pure ice latent heat of sublimation	2834×10^3	$J\ kg^{-1}$
μ	Sea ice melting point coefficient	0.054	$\permil °C^{-1}$
β_1	First thermal conductivity coefficient	0.09	$W\ m^{-1}\ \permil^{-1}$
β_2	Second thermal conductivity coefficient	0.011	$W\ m^{-1}\ K^{-2}$
ϵ	Sea ice surface emissivity	0.97	–
S^G	Winter equilibrium sea ice salinity	5	$\permil$
S^F	Summer equilibrium sea ice salinity	2	$\permil$
S^1	First salinity transition coefficient	3.5	$\permil$
S^2	Second salinity transition coefficient	4.5	$\permil$
T^G	Winter sea ice salinity time scale	20	days
T^F	Summer sea ice salinity time scale	10	days

The present contribution focuses on one of the aforementioned large-scale sea ice models: LIM3. LIM[2] is originally a sea ice model developed by Fichefet and Morales Maqueda (1997), including ice dynamics based on the VP rheology (Hibler, 1979) and 3-layer ice thermodynamics (Semtner, 1976). The basis of the coupling with ocean models was introduced by Goosse and Fichefet (1999). LIM (which we will refer to as LIM1 in the remainder of the text) was then coupled to the ocean model OPA[3] v8.2, leading to the ice–ocean model configuration ORCA2-LIM[4] (Timmermann et al., 2005). The code was then rewritten formally[5] without any significant physical change, which resulted in LIM2. More recently, as the relatively simple ice physics in LIM1 and LIM2 were suspected to induce biases in the simulation of the sea ice features, the development of a new version of the model, LIM3, was initiated. LIM3 includes three major improvements: a C-grid elastic–viscous–plastic rheology, several categories of ice thickness and multi-layer halo-thermodynamics.

Hereafter, in the first part of this twofold paper, we describe and test LIM3. LIM3 is included in the ocean modelling system NEMO[6], which includes the latest version of OPA. Our purpose is (1) to document model behavior (in particular the improvement compared with prior versions associated with the main originalities of LIM3) and (2) to identify the main shortcomings and orient future research. To accomplish this goal, we analyze the results of LIM3 in a 1970–2006 hindcast performed with NEMO–LIM3 and compare them with several sets of observational data. In the companion paper (Vancoppenolle et al., 2009), we focus on the importance of the sea ice salinity processes.

---

[1] IPCC = Intergovernmental Panel on Climate Change.

[2] LIM = Louvain-la-Neuve sea Ice Model, developed at the Institut d'Astronomie et de Géophysique Georges Lemaître, Louvain-la-Neuve, Belgium.
[3] OPA = Océan Parallélisé, developed at LOCEAN, Paris, France.
[4] ORCA2-LIM is a configuration of the OPA model.
[5] LIM2 was written by Christian Ethé and Gurvan Madec at LOCEAN.
[6] NEMO = Nucleus for European Modelling of the Ocean.

2. Model description

The model used in this study is a global coupled ice–ocean model that consists of the ice model LIM3, a C-grid dynamic–thermodynamic sea ice model with thickness, enthalpy, salinity and age distributions, and the ocean model OPA v9.0 (Madec, 2008), in the framework of the NEMO ocean modelling system. The representation of sea ice is done through a velocity vector and a series of ice state variables described further below. A list of model parameters and constants is given in Table 1.

2.1. Ocean general circulation model

OPA is a finite difference, hydrostatic, primitive equation ocean general circulation model, with a free surface and a non-linear equation of state in the Jackett and McDougall (1995) formulation. Lateral tracer mixing is done along isopycnals. Eddy-induced tracer advection is parameterized following Gent and McWilliams (1990) with the thickness diffusivity decreased in the tropics. Partial steps, i.e., specifying the depth of the bottom cell variable and adjustable to the real depth of the ocean (Pacanowski and Gnanadesikan, 1998), induce a better representation of steep topographic gradients and oceanic general circulation (Barnier et al., 2006). Surface boundary layer mixing and interior vertical mixing are parameterized according to a turbulence closure model (order 1.5) adapted to OPA by Blanke and Delecluse (1993). In case of static instability, a viscosity/diffusivity enhancement up to 10 m² s⁻¹ is used.

2.2. Ice dynamics

The ice velocity **u** is determined from the momentum balance:

$$m \frac{\partial \mathbf{u}}{\partial t} = \boldsymbol{\tau}_a + \boldsymbol{\tau}_w - mf\mathbf{k} \times \mathbf{u} - mg\nabla\eta + \nabla \cdot \boldsymbol{\sigma}, \qquad (1)$$

where m is the mass of snow and ice par unit area, $\boldsymbol{\tau}_a$ and $\boldsymbol{\tau}_w$ are the contributions of air and water stresses and $\nabla \cdot \boldsymbol{\sigma}$ is the internal stress term. f, g, η and **k** are the Coriolis parameter, the acceleration of gravity, the sea surface elevation and a unit vector pointing upwards, respectively. Scale analysis shows that advection is at least one order of magnitude smaller than the acceleration term (Oberhuber, 1993) and therefore, negligible.

Eq. (1) assumes that sea ice is a two-dimensional VP continuum, following Hibler (1979), with an elliptical yield curve aspect ratio $e = 2$. The momentum equation is solved using the new C-grid formulation (Bouillon et al., 2009) of EVP (Hunke and Dukowicz, 1997). We use 300 sub-iterations for ice dynamics, so that the time step used in the dynamic component is $\Delta t_{\mathrm{dyn}} = 96$ s. An artificial regularization of small strain rates is made by introducing damped elastic waves, with the damping time scale set to 9760 s, which is high enough to ensure model stability (Hunke, 2001) and small enough so that elastic waves are damped when ice dynamics have converged. The stress tensor at the end of each time step is used at the beginning of the next iteration, which improves convergence and global model stability. The invariants of the stress tensor used to force the mechanical redistribution module are computed at the end of the dynamic time step. For the ice strength, we follow Hibler (1979) formulation and use $P^* = 40{,}000$ Nm⁻¹, which lies in the 30,000–45,000 Nm⁻¹ range proposed by Tremblay and Hakakian (2006) based on satellite data.

Compared to the former B-grid VP rheology, experiments with LIM2 show that EVP has higher stability and responds more rapidly to changes in the wind forcing (Hunke and Zhang, 1999). Because it allows to drastically reduce the numerical viscous flow limit, using EVP gives a better solution of the ice momentum equation. Moreover, EVP is explicit, which allows easier parallelization. Furthermore, because the grid size is much smaller than the sea ice

deformation radius, the C-grid has better dispersion properties than a B-grid (Bouillon et al., 2009). In addition, straits are better represented. Finally, the coupling to the OPA model (written on a C-grid) is straightforward. Nevertheless, the C-grid requires the interpolation of velocities in order to calculate the Coriolis term.

2.3. Ice state variables

The thickness distribution is numerically discretized into several ice thickness categories. The numerical formulation of the thickness categories follows Bitz et al. (2001) and Lipscomb (2001). A fixed number M of thickness categories ($M = 5$) is imposed. Each thickness category has a mean thickness h_m^i ($m = 1$, 2, ..., M) which is constrained to lie between H_{m-1} and H_m. H_0 is set to zero. The other boundaries are chosen with greater resolution for thin ice (see Fig. 1). Sea ice in each category is divided into N vertical layers of ice and one layer of snow.

Each ice category has its own set of global state variables (see Table 2 for a list). The global ice state variables are extensive variables which include the ice concentration (g_m^i), the ice volume per unit area (v_m^i), the ice enthalpy per unit area ($e_{m,k}^i$, $k = 1, 2, ..., N$), the ice salt content (M_m^s), the ice age content (O_m), as well as the snow volume per unit area (v_m^s) and the snow enthalpy per unit area (e_m^s). The global state variables are used by all but thermodynamic model routines, in which they are, for convenience, converted into equivalent state (intensive) variables (i.e., thickness, temperatures, ...; see Table 3 for a list). In the remainder of the text, the m index runs for ice thickness categories and k for the vertical ice layers.

The global ice variables undergo changes that are classified into changes due to transport, thermodynamic and mechanical redistribution processes. Extending Eqs. (4)–(6) of Bitz et al. (2001), we
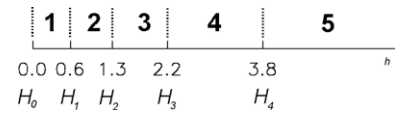

Fig. 1. Boundaries of the model ice thickness categories (m).

Table 2
Sea ice state variables in LIM3.

Symbol	Description	Units
u	Sea ice velocity	[m s⁻¹]
g_m^i	Concentration of sea ice in category m	[–]
v_m^i	Volume of sea ice per unit area in category m	[m]
v_m^s	Volume of snow per unit area in category m	[m]
$e_{m,k}^i$	Sea ice enthalpy per unit area in category m and layer k	[J m⁻²]
e_m^s	Snow enthalpy per unit area in category m	[J m⁻²]
M_m^s	Sea ice salt content in category m	[‰ m]
O_m	Sea ice age content in category m	[days m]

Table 3
Equivalent variables in LIM3. To each state variable corresponds an equivalent variable. Equivalent variables are used only in 1-D modules.

Symbol	Description	Units
$h_m^i = v_m^i / g_m^i$	Ice thickness	[m]
$h_m^s = v_m^s / g_m^i$	Snow depth	[m]
$q_{m,k}^i = e_{m,k}^i / (h_m^i / N)$	Ice specific energy of melting	[J m⁻³]
$q_m^s = e_m^s / h_m^s$	Snow specific energy of melting	[J m⁻³]
$T_{m,k}^i = T(q_{m,k}^i)$	Ice temperature	[K]
$T_m^s = T(q_m^s)$	Snow temperature	[K]
$S_m^i = M_m^s / v_m^i$	Ice salinity	[‰]
$o_m^i = O_m / v_m^i$	Ice age	[days]

impose that all the global ice state variables (X) follow a conservation equation of the form:

$$\frac{\partial X}{\partial t} = -\nabla \cdot (X\mathbf{u}) + \Psi^X + \Theta^X, \tag{2}$$

where Θ^X and Ψ^X represent the effects of thermodynamical and mechanical redistribution processes on X, respectively.

2.4. Transport

As in Fichefet and Morales Maqueda (1997), the global ice state variables are transported horizontally using the advection scheme of Prather (1986). This scheme is based on the conservation of second-order moments of the advected quantity. It is weakly diffusive and avoids unphysical negative values.

2.5. Mechanical redistribution

Divergence and shear open the ice pack and create ice of zero thickness. Convergence and shear consume thin ice and create thicker ice by mechanical deformation through rafting (piling of two ice sheets on top of each other) and ridging (piling of a series of broken ice blocks into ridges). The redistribution functions Ψ^X describe how opening and deformation affect the global ice state variables. In the model, they depend on the strain rate tensor and the thickness distribution itself.

2.5.1. Main redistribution function

A general expression of Ψ^g, the mechanical redistribution function associated with the ice concentration, was proposed by Thorndike et al. (1975):

$$\Psi^g = |\dot{\epsilon}| [\alpha_o(\theta)\delta(h) + \alpha_d(\theta)w_d(h,g)], \tag{3}$$

The first and second terms on the right-hand side correspond to opening and deformation, respectively. $|\dot{\epsilon}| = (\dot{\epsilon}_I^2 + \dot{\epsilon}_{II}^2)^{\frac{1}{2}}$, $\dot{\epsilon}_I$ and $\dot{\epsilon}_{II}$ are the strain rate tensor invariants, $\theta = \text{atan}(\dot{\epsilon}_{II}/\dot{\epsilon}_I)$ and $w_d(h,g)$ is the deforming mode. $|\dot{\epsilon}| \alpha_o$ and $|\dot{\epsilon}| \alpha_d$ are the lead opening and closing rates, respectively, and they are related by $|\dot{\epsilon}| \alpha_o - |\dot{\epsilon}| \alpha_d = |\dot{\epsilon}_I|$. The closing rate can be written as a sum of two terms representing the energy dissipation by shear and convergence (Flato and Hibler, 1995):

$$|\dot{\epsilon}| \alpha_d(\theta) = C_s \frac{1}{2}(\Delta - |\dot{\epsilon}_I|) - \min(\dot{\epsilon}_I, 0), \tag{4}$$

where $\Delta = (\dot{\epsilon}_I^2 + \dot{\epsilon}_{II}^2/e^2)^{\frac{1}{2}}$ for an elliptical yield curve. The factor C_s is added to allow for energy sinks other than ridge building (e.g., sliding friction) during shear.

Babko et al. (2002) concluded that rafting plays a significant role during initial ice growth in fall. Therefore, we assume that the deforming mode consists not only of ridging (which redistributes participating ice on a wide range of thicknesses) but also rafting (which doubles the participating ice thickness):

$$w_d(h,g) = -[b^{ra}(h) + b^{ri}(h)]g(h) + n^{ra}(h) + n^{ri}(h), \tag{5}$$

where $b^{ra}(h)$ and $b^{ri}(h)$ are the rafting and ridging participation functions. They determine which regions of the ice thickness space participate in the redistribution. $n^{ra}(h)$ and $n^{ri}(h)$, called transfer functions, specify how thin, deforming ice is redistributed onto thick, deformed ice. Participation and transfer functions are normalized in order to conserve area.

2.5.2. Participation functions

We assume that the participation of ice in redistribution does not depend on the deformation process going on (rafting or ridging). Therefore, the participation functions can be written as follows:

$$b^{ra}(h) = \beta(h)b(h), \tag{6}$$

$$b^{ri}(h) = [1 - \beta(h)]b(h), \tag{7}$$

where $b(h)$ is an exponential weighting function with an e-folding scale a^* (Lipscomb et al., 2007), which preferentially apportions the thinnest available ice to ice deformation. It is numerically more stable than the original version of Thorndike et al. (1975). $\beta(h)$ partitions deforming ice between rafted and ridged ice. It is formulated following Haapala (2000), using the Parmerter (1975) law, which states that, under a critical participating ice thickness h_P, ice rafts, otherwise it ridges:

$$\beta(h) = \frac{tanh[-C_{ra}(h - h_P)] + 1}{2}, \tag{8}$$

where $C_{ra} = 5 \text{ m}^{-1}$ and $h_P = 0.75 \text{ m}$ (Haapala, 2000; Babko et al., 2002). The *tanh* function is used to smooth the transition between ridging and rafting. In spite of its relative simplicity (see, e.g., Tuhkuri and Lensu, 2002), our formulation constitutes a step towards a better representation of mechanical redistribution in models.

2.5.3. Transfer functions

The rafting transfer function assumes a doubling of ice thickness:

$$n^{ra}(h) = \frac{1}{2} \int_0^\infty \delta(h - 2h')b(h')g(h')dh', \tag{9}$$

where δ is the Dirac delta function, while the ridging transfer function is:

$$n^{ri}(h) = \int_0^\infty \gamma(h', h)(1 + p)b(h')g(h')dh'. \tag{10}$$

The redistributor $\gamma(h', h)$ specifies how area of thickness h' is redistributed on area of thickness h. We follow Hibler (1980) who constructed a rule, based on observations, that forces all ice participating in ridging with thickness h' to be linearly distributed between ice that is between $2h'$ and $2\sqrt{H^*h'}$ thick, where $H^* = 100 \text{ m}$. This in turn determines how to construct the ice volume redistribution function Ψ^v. Volumes equal to participating area times thickness are removed from each participating thin ice category. They are redistributed following Hibler's rule. The factor $(1 + p)$ accounts for initial ridge porosity p, defined as the fractional volume of seawater initially included into ridges. In many previous models, the initial ridge porosity has been assumed to be 0, which is not the case in reality since newly formed ridges are porous. In situ observations suggest that p is about 0.3 (Leppäranta et al., 1995; Høyland, 2002). In summary, compared to the case with $p = 0$, LIM3 produces a larger volume of ridged ice with the same amount of participating ice.

2.5.4. Mechanical redistribution for other global ice variables

The other global ice state variables redistribution functions Ψ^X are computed based on Ψ^g for the ice age content and on Ψ^{v^i} for the remainder (ice enthalpy and salt content, snow volume and enthalpy). The general principles under this derivation are described in Appendix A of Bitz et al. (2001). The peculiarities of the scheme used here are the following. A fraction $f_s = 0.5$ of the snow volume and enthalpy is assumed to be lost during ridging and transferred to the ocean. The contribution of the seawater trapped into the porous ridges is included in the computation of the redistribution of ice enthalpy and salt content (i.e., Ψ^{e^i} and Ψ^{M^s}). During this computation, seawater is supposed to be in thermal equilibrium with the surrounding ice blocks. The inclusion of seawater in ridges does not imply any net change in ocean salinity. The heat lost to cool the

seawater trapped in porous ridges until the seawater freezing point is given to the ocean. Ridged ice desalination induces an implicit decrease in internal brine volume, and a heat supply to the ocean, which accounts for ridge consolidation as described by Høyland (2002).

2.5.5. Role of ridge porosity and rafting

Sensitivity experiments indicate that assuming a non-zero ridge porosity increases the mean simulated Northern Hemisphere ice volume by a few percent, which suggests that an additional melt of the warm porous ridges compensates for the additional ice volume created initially. No significant difference is found in the Southern Hemisphere.

Including rafting in the model increases the total average simulated ice volume in the Southern Hemisphere by 25%. In this region, thinner rafted ice occupies more area than thicker ridged ice, in particular in the winter–spring marginal ice zone. In spring, less solar radiation is absorbed and less basal melt occurs than if only ridging is included, which leads to a summer ice extent larger by 1×10^6 km². In the Northern Hemisphere, where the deformed ice volume is higher, thinner rafted ice results only in a 2% decrease in the simulated ice volume.

2.6. Ice thermodynamics

The thermodynamic processes (Θ^X) include vertical diffusion of heat in the snow/ice system, snow/ice growth and decay, creation of new ice in open water, brine drainage and ice natural ageing. After thermodynamics are computed, the linear remapping scheme of Lipscomb (2001), which computes the transport in thickness space among categories due to ice growth/melt, is applied to all state variables. This scheme is weakly diffusive, converges with a few thickness categories and its computational cost is minimal. In LIM3, there is no explicit account for lateral melting. Lateral melting is controlled by floe size (Steele, 1992), which is not a model variable. Nevertheless, as in other models including ITD, there is some implicit lateral melting accounted for by the melt of thin ice (Bitz et al., 2001).

2.6.1. Vertical growth and decay

The formulation of ice vertical thermodynamics follows Bitz and Lipscomb (1999) and VBF07. Vertical heat conduction and storage and vertical temperature profile in sea ice are governed by a 1-D heat diffusion equation. Surface energy balance and seawater freezing point provide the boundary conditions at the top and bottom interfaces, respectively. The albedo is a function of the state of the surface, ice thickness and snow depth (Shine and Henderson-Sellers, 1985). A fraction i_0 of the shortwave radiation absorbed at the surface, function of cloudiness, is transmitted inside the ice, as in Fichefet and Morales Maqueda (1997). Radiation is absorbed in the ice cover following Beer's law, with an attenuation coefficient $\kappa_i = 1$ m^{-1}. Radiation does not penetrate into snow. For each thickness category, the heat diffusion equation is solved in the snow–ice system, using one layer of snow and $N = 5$ layers of ice. We noticed that this number can decrease until 2 without significantly deteriorating the results. The imbalance between external and inner heat conduction fluxes at the interfaces are used to compute growth/melt rates. The salinity evolution is then computed. Finally, to account for changes in ice/snow thickness and salinity in an energy-conserving way, the new temperature profile is remapped on the updated vertically uniform grid.

2.6.2. Brine pockets

The impact of brine pockets on heat transfer and storage is done following Maykut and Untersteiner (1971) and Bitz and Lipscomb (1999), by formulating sea ice thermal properties as functions of

salinity S (in ‰) and temperature T (in °C). The sea ice specific heat is given by (Malmgren, 1927):

$$c_i(S, T) = c_0 + L_0 \mu \frac{S}{T}, \tag{11}$$

where c_0 and L_0 are the specific heat and latent heat of fusion of fresh ice, respectively, and μ is an empirical constant relating the seawater freezing point to its salinity $T_m = -\mu S$. The sea ice thermal conductivity follows Pringle et al. (2007):

$$k_i(S, T) = k_0 + \beta_1 \frac{S}{T} - \beta_2 T, \tag{12}$$

where k_0 is the thermal conductivity of pure ice and β_1 and β_2 are empirical constants. Following Bitz and Lipscomb (1999), we assume that the sea ice specific energy of melting q (i.e., the energy required to melt a unit volume of sea ice) is also a function of salinity and temperature:

$$q(S, T) = \rho_i c_0 (-\mu S - T) + \rho_i L_0 \left(1 + \frac{\mu S}{T}\right) + c_w \mu S, \tag{13}$$

where ρ_i is the pure ice density and c_w the specific heat of seawater. The enthalpy per unit area in any ice layer of thickness $\Delta h = h_i/N$ is $q(S,T)\Delta h$. With such a formulation, saline ice grows more than fresh ice for a given heat loss.

2.6.3. Sources and sinks of ice mass

Ice mass can be created by congelation growth at the ice base, by new ice growth in open water areas and by snow ice formation. Ice mass can be lost by melting at the top and bottom interfaces.

Basal growth. If heat is lost at the ice base, ice grows. The ice growth rate in the mth category is given by:

$$\frac{\partial h_m^{i,b+}}{\partial t} = -\frac{F_m^b}{q\left(S_m^{i,b}, T^w\right)}, \tag{14}$$

where F_m^b is the heat loss at the bottom surface in the mth category. T^w is the ice–ocean interface temperature, which is equal to the seawater freezing point. $S_m^{i,b}$, the salinity of new ice in the mth category, is given by:

$$S_m^{i,b} = \nu \left(\frac{\partial h_m^{i,b+}}{\partial t}\right) S^w, \tag{15}$$

where ν is a fractionation coefficient depending on ice growth (Cox and Weeks, 1988) and S^w is the sea surface salinity. The system of three nonlinear Eqs. (13)–(15) is solved iteratively. The associated enthalpy per unit area is added at the ice base.

Snow ice. The formation of snow ice results from the transformation of snow into ice at the snow–ice interface. As in Fichefet and Morales Maqueda (1997), we assume that when snow is thick enough to depress the snow–ice interface below the sea level, seawater infiltrates and refreezes into the snow, so that snow ice formation occurs:

$$\Delta h_m^{si} = \frac{\rho_s h_m^s - (\rho_w - \rho_i) h_m^i}{\rho_s + \rho_w - \rho_i}, \tag{16}$$

where ρ_w and ρ_s are the reference densities of seawater and snow, respectively. The newly created ice is assumed to have $T = T^w$ and $S = S^{si} = (\rho_i - \rho_s)/\rho_i S^w$. A corresponding enthalpy per unit area $q(S^{si}, T^w)\Delta h_m^{si}$ is added on top of the sea ice surface and merged with the remainder of the sea ice column. The residual energy (used to warm the snow until T^w) is removed from the top ocean layer. In the model, snow ice formation is assumed instantaneous, though in reality, surface flooding leads to either snow ice or slush layers (see, e.g., Haas et al., 2001). There is work under way to improve the representation of surface flooding.

Ice melt. Ice melts following a convergence of heat. The ice melt rate at the top and bottom interfaces in the mth category is computed by solving $\partial h_m^{i-}/\partial t = -F_m/q(S_N, T_N)$, where F_m is the net heat flux, computed from the difference between external fluxes and internal conductive heat flux. $q(S_N, T_N)$ is the energy of melting of the interfacial ice layer.

New ice formation. If the top ocean layer is at its freezing point and the surface is losing heat, new ice forms. Ice forming in open water has a thickness h^0 and a volume given by:

$$\frac{\partial v^{i,0}}{\partial t} = -\frac{F^{ow}}{q(S^0, T^w)},\tag{17}$$

where F^{ow} is the heat loss in open water areas. The salinity of new ice S^0 is a function of ice thickness, following the observation-based regression of Kovacs (1996):

$$S^0 = 4.606 + \frac{0.91603}{h^0}.\tag{18}$$

h^0, also sometimes called frazil ice collection thickness, represents the thickness of new ice formed during a time step. h^0 is computed in both hemispheres using a parameterization based on Biggs et al. (2000). In this parameterization, the conservation of momentum and energy of the frazil–pack ice system gives the thickness of new ice as a nonlinear function of ice velocity, wind speed and pack ice thickness. It gives new ice thicknesses ranging from 5 to 15 cm. Finally, the fractional area of new ice is diagnosed using the relation $dA^0 = dv^{i,0}/h^0$, and new ice (i.e., all its state variables) is merged in the category where h^0 stands. This category has generally $m = 1$. The computed value of h^0 is well suited for the representation of new ice growth in the calm waters of the Arctic Ocean, as well as for leads and polynyas, but is not ideal for dynamical (pancake) ice growth processes in turbulent conditions, prevalent in the Southern Ocean marginal ice zones.

2.6.4. Snow

Snow has constant density, specific heat, thermal conductivity and latent heat, one temperature point and no salinity. Snow depth increases when snow falls and decreases by snow ice formation, sublimation and melt. Clearly, the representation of snow is simple and should be improved in future model versions.

2.6.5. Salinity variations

The global sea ice state variable associated with the ice salinity in the mth category is the sea ice salt content $M_m^s = S_m^i v_m^i$, where S_m^i is the vertically averaged (hereafter referred to as "bulk") sea ice salinity in the mth category. The evolution of M_m^s follows an equation similar to (2). Θ^{M^s} includes (1) brine entrapment and drainage and (2) transport in thickness space due to ice growth/melt.

The representation of brine entrapment and drainage is based on a simplification of the more complex VBF07 model. Field data (Malmgren, 1927), laboratory experiments (Cox and Weeks, 1975) and 1-D simulations with the VBF07 model (Vancoppenolle et al., 2006) indicate that the sea ice desalination can be divided into initial, winter and summer stages. Gravity drainage and flushing dominate winter and summer desalinations, respectively. In addition, salinity data from ice cores drilled in some of the Southern Ocean deep snow-covered regions suggest that salt concentration occurs at the ice surface during snow ice formation (Jeffries et al., 1997). Therefore, in the thermodynamic module, the following equation for S_m^i is solved:

$$\frac{\partial S_m^i}{\partial t} = \frac{vS^w - S_m^i}{h_m^i}\frac{\partial h_m^{i,b+}}{\partial t} + \frac{S^{si} - S_m^i}{h_m^i}\frac{\partial h_m^{i,si}}{\partial t} - \left(\frac{S_m^i - S^G}{T^G}\right)I^G - \left(\frac{S_m^i - S^F}{T^F}\right)I^F.\tag{19}$$

The terms on the right-hand side refer to brine entrapment during ice growth, snow ice formation, gravity drainage and flushing, respectively. T^G and S^G (T^F and S^F) are the winter (summer) desalination time scale and equilibrium salinity. $I^G = 1$ if the temperature is warmer at the ice base than at the surface, i.e., in winter, and 0 otherwise. Since brine salinity increases towards low temperatures, a temperature gradient directed downwards leads to an unstable brine density gradient in the brine network, which triggers desalination (Cox and Weeks, 1988). $I^F = 1$ if surface melts and 0 otherwise. This parameterization implicitly contains a simple representation of the *flood–freeze cycle* (Lytle and Ackley, 1996; Fritsen et al., 1998), i.e., the incorporation of salty seawater at the snow–ice interface associated with snow overload and seawater flooding, and its subsequent removal by convection through the open brine network. In the model, first, salt is incorporated at the ice surface during snow ice formation (flooding). Second, the excess of salt is then removed by the sink term associated to gravity drainage, representing the effect of convection. The flood–freeze cycle presumably occurs in most of the Southern Ocean ice-covered areas.

We assume that salinity has a vertical distribution $S_{m,k}^i(z_{m,k})$ only in thermodynamic computations. $Z_{m,k}$ is the vertical coordinate of the midpoint of the kth layer in the mth category, referenced to the snow–ice interface. Observation of the vertical sea ice salinity profile from ice cores suggests that the shape of the profile is a function of the bulk ice salinity because flushing affects both the mean salinity and profile shape (VBF07). Numerical experiments have shown that a linear profile well approximates the sea ice salinity profile (Vancoppenolle et al., 2005). Therefore, we assume the following. At high mean salinity, i.e., if $S_m^i > S^2 = 4.5‰$, the profile is isosaline: $S_{m,k}^i = S_\infty(z_{m,k}) = S_m^i$. At low mean salinity, i.e., if $S_m^i < S^1 = 3.5‰$, the profile is linear and constrained, first, by its mean salinity, equal to S_m^i, which is given by (19) and, second, by $S = 0‰$ at the surface:

$$S_{m,k}^i = S_0(z_{m,k}) = 2\frac{S_m^i}{h_m^i}z_{m,k}.\tag{20}$$

At intermediate salinities, i.e., between S^1 and S^2, $S_{m,k}^i$ is a combination of S_0 and S_∞. In summary,

$$S_{m,k}^i(z) = \alpha(S_m^i)S_0(z_{m,k}) + \left[1 - \alpha\left(S_m^i\right)\right]S_\infty(z_{m,k}),\tag{21}$$

where

$$\alpha\left(S_m^i\right) = \begin{cases} 1 & \text{if} \quad S_m^i < S^1 \\ (S_m^i - S^2)/(S^1 - S^2) & \text{if} \quad S^1 \leqslant S_m^i \leqslant S^2 \\ 0 & \text{if} \quad S_m^i > S^2. \end{cases}$$

Local thermodynamic equilibrium is assumed during brine drainage. Therefore, an increase in temperature compensates any desalination. The relative brine volume $e_{m,k}$ can be diagnosed from salinity and temperature using the relation $e_{m,k} = -\mu S_{m,k}/T_{m,k}$.

2.7. Ice age

For diagnostic purposes, the ice age o_m^i of each thickness category is computed. The use of age in marine modelling has shown that the values and interpretation of model age are strongly dependent on the age definition (see, e.g., Deleersnijder et al., 2001), stressing the importance of the latter. We assume that the age is associated with the areal sea ice age content $O_m = o_m^i g_m^i$, which verifies:

$$\frac{\partial O_m}{\partial t} = -\nabla \cdot (O_m \mathbf{u}) + \Theta_m^O + \Psi_m^O.\tag{22}$$

For coherence, first, the mechanical redistribution function associated with ice age, Ψ^O, is constructed based on Ψ^g (see earlier). Second, in contrast to Harder and Lemke (1994), vertical growth and melt do not affect the ice age (i.e., vertically accreted new ice is assumed to have the age of existing ice). Nevertheless, new ice formed in open water has an age equal to zero. Therefore, our value reflects an areal residence time, larger than the actual ice age, and the thermodynamic ageing term reads:

$$\Theta_m^O = g_m^i - \frac{\partial(f_m O_m)}{\partial h}, \tag{23}$$

where f_m is the sea ice growth/melt rate in the mth category. The first term on the right-hand side represents ice ageing. The second term accounts for the formation of new ice in open water and for the transport in thickness space of the age content due to ice growth and melt.

2.8. Ice–ocean coupling

The ice–ocean coupling is conceptually similar to Goosse and Fichefet (1999). Ice and ocean exchange momentum through an ice–ocean stress deriving from a quadratic bulk formula assuming an oceanic drag coefficient of $C_w = 5.0 \times 10^{-3}$. Differences in sea surface elevation are neglected here but will be activated in future model versions.

The oceanic heat flux, function of the temperature of the ocean and turbulent mixing, derives from McPhee (1992) and Goosse and Fichefet (1999):

$$F_w = \rho_w c_w C_h u_{io}^*(T^w - T^{oc}), \tag{24}$$

where $C_h = 0.006$ is a heat transfer coefficient (McPhee, 1992), T^{oc} is the sea surface temperature and u_{io}^* is the friction velocity, which depends on the ice–ocean root mean square velocity difference.

Freshwater fluxes for ocean and sea ice use the approach of Tartinville et al. (2001). Adaptations were made to account for time-varying sea ice salinity. From Tartinville et al. (2001), we adopt the following convention. First, if liquid or solid water is added to or extracted from the ice–ocean system (e.g., through precipitation or evaporation), then it is introduced as a freshwater flux. Second, if a surface process affects ocean salinity without a net gain or loss of water for the ice–ocean system (e.g., through ice melting or freezing), this internal exchange is transformed into an equivalent salt flux that is applied to the ocean. In this approach, sea ice acts as a negative reservoir of salt inside the ice–ocean system. When ice forms, some salt is released into the ocean. As ice melts, salt is taken out of the ocean.

The freshwater flux at the surface of the ocean F^f (in kg/m^2/s) is given by:

$$F^f = P - E + R - \frac{\rho_s}{\rho_w}\sum_{m=1}^{M}\frac{\partial v_m^{s,-}}{\partial t}, \tag{25}$$

where P is the precipitation, E the evaporation, R the river runoff, $\partial v_m^{s,-}/\partial t$ is the snow volume loss per unit area in the mth category due to snow melt and snow ice formation. The salt flux F^s reads:

$$F^s = F_b^s + F_{eq}^s. \tag{26}$$

F_b^s is the salt flux due to brine drainage:

$$F_b^s = \rho_i \sum_{m=1}^{M} v_m^i \left(\frac{\partial S_m^i}{\partial t}\Big|_G + \frac{\partial S_m^i}{\partial t}\Big|_F\right). \tag{27}$$

The partial derivatives on the right-hand side refer to the loss of salt by gravity drainage and flushing (next-to-last and last terms of (19)), respectively. F_{eq}^s is the equivalent salt flux due to ice growth and melt:

$$F_{eq}^s = \rho_i(S^w - S^n)\frac{\partial v^{i,n}}{\partial t} + \rho_i \sum_{m=1}^{M} g_m^i \left[\left(S^w - S_m^{i,b}\right)\frac{\partial h_m^{i,b+}}{\partial t}\right.$$
$$\left. + \left(S^w - S_m^{si}\right)\frac{\partial h_m^{i,si}}{\partial t} + \left(S^w - S_m^i\right)\frac{\partial h_m^{i,-}}{\partial t}\right]. \tag{28}$$

The terms on the right-hand side correspond to the salt rejected during new ice formation in open water, to basal congelation growth, to snow ice formation and to the melt of saline ice, respectively.

3. Forcing and experimental design

3.1. Model grid

The ocean and sea ice models both run over the same domain, extending from 78°S to 90°N. The model uses the tripolar ORCA2 grid with 2° zonal resolution and a meridional resolution varying from 0.5° at the equator to $2° \cos\phi$ at a latitude ϕ (see Timmermann et al., 2005 and Madec, 2008; for details). The grid features two points of convergence in the Northern Hemisphere, both situated on continents. The ocean model has a time step of $\Delta t_o = 5760s = 1/15$ day and the ice model is called every five ocean time steps ($\Delta t_i = 28,800 s = 1/3$ day).

3.2. Simulation setup

The simulation is conducted over the period 1948–2006. Unless otherwise stated, years 1979–2006 – for which satellite data are available – are analyzed. The initial ocean temperature and salinity fields are specified using the January data from the Polar Science Center Hydrographic Climatology (PHC, Steele et al., 2001). Initial mean sea ice thicknesses (snow depths) of 3.5 m (0.3 m) in the Arctic and 1 m (0.1 m) in the Southern Ocean are imposed in regions with a sea surface temperature below 0 °C. Initial ice concentration is assumed to be 0.95 (0.90) in the Arctic (Antarctic). Initially, the ice thickness distribution is assumed to be Gaussian, age and velocity are prescribed to 0, salinity to 6‰ and ice and snow temperatures to 270 K.

3.3. Model forcing

Atmospheric forcing fields are a combination of NCEP/NCAR daily reanalysis data of 10-m wind speed and 2-m temperature (Kalnay et al., 1996), and monthly climatologies of relative humidity (Trenberth et al., 1989), total cloudiness (Berliand and Strokina, 1980) and precipitation (Large and Yeager, 2004).

Reanalysis and climatological data are interpolated from a $2° \times 2°$ latitude–longitude grid to the ORCA2 grid with a 3rd-order moment conserving algorithm and interpolated linearly in time to get a value at each oceanic time step. Surface radiative and turbulent heat fluxes are calculated as in Goosse (1997). Surface wind stress derives from quadratic bulk formulae assuming an atmospheric drag coefficient of $C_a = 1.40 \times 10^{-3}$. Evaporation/sublimation is derived from the latent heat flux. River runoff rates are prescribed using the climatological dataset of Baumgartner and Reichel (1975) combined with a mean seasonal cycle derived from the Global Runoff Data Centre (GRDC) data.

Contrary to earlier versions of the model, no restoring for sea surface salinities is used. This is due to the better large-scale Arctic sea ice distribution which induces a reduction in the freshwater export through Fram Strait and improves the simulated oceanic thermohaline circulation (THC) in the model (see Section 4.4.2).

4. Results

In this section, we discuss the simulated ice areal coverage, volume and drift, the snow volume, and the ice age and salinity fields.

We compare the model results with available observations and to LIM1 and AOMIP (Arctic Ocean Model Intercomparison Project) hindcast simulations. The LIM1 control simulation setup and forcing configuration is similar to the LIM3 simulation discussed hereafter, except that the run spans two times the 1977–1999 period, and that an older precipitation dataset is used (see Timmermann et al., 2005). LIM1 is a single-category model with VP dynamics and Semtner (1976) 3-layer thermodynamics. The AOMIP (see Johnson et al., 2007 and Gerdes and Köberle, 2007) simulations are a series of 1948–2001 hindcast runs with nine different ice–ocean models, including several physical parameterizations at various spatial resolutions. There is not yet an equivalent intercomparison project in the Southern Hemisphere.

4.1. General view of the ice physical state

The physical state of the winter ice cover is summarized in Fig. 2 and several statistics of the simulation are shown in Table 4. The model simulates significantly different ice packs in the Northern and Southern Hemispheres (hereafter referred to as NH and SH). Arctic ice is on average (1979–2006) older (2.6 years) than its Antarctic counterpart (100 days). Therefore, it is also thicker (1.91 m in the NH vs. 42 cm in the SH), has a deeper snow cover (24 cm vs. 18 cm), is less saline (3.6‰ vs. 6.3‰) and has a lower brine volume (6.3% vs. 7.5%). The sources and sinks of ice mass also differ markedly (see Section 4.3.3). This is in good correspondence with in situ observations of ice thickness and snow depth, and textural analysis of ice cores from the Arctic and Antarctic regions (see, e.g., Tucker et al., 1987; Eicken, 1998).

4.2. Ice areal coverage

In this subsection, the mean seasonal cycle and interranual variations of the hemispheric ice coverage as well as the geographical distribution of ice concentration are discussed.

4.2.1. Mean seasonal cycle

Averaged over 1979–2006, in the NH, the simulated maximum (minimum) hemispheric area is equal to 14.2 (4.4) $\times 10^6$ km^2, and is reached on Feb 23 (Aug 26). The mean seasonal cycle of ice area and the maximum (Fig. 3) closely match the Bootstrap PMW recordings (Comiso, 2007). The minimum area is however underestimated by 1×10^6 km^2 and is reached 15 days earlier than observed. The ice extent (i.e., the area enclosed within the 15% concentration contour) is underestimated all year long by 1–1.5 $\times 10^6$ km^2. In the SH, the area maximum (minimum) is 19.5 (0.9) $\times 10^6$ km^2 and is reached on Aug 15 (Feb 15). The seasonal cycle is reasonably well represented. Areal growth is faster than observed. The maximum area is reached 20 days in advance and is significantly overestimated, by 2.5 $\times 10^6$ km^2. The simulated seasonal cycle of ice extent is much more realistic. This reflects the fact that the model SH ice concentration is higher than in the observations.

4.2.2. Spatial distribution

The ice edge is well simulated by the model in both hemispheres and the geographical distributions of ice concentration are in good agreement with observations from the Bootstrap data set (Comiso, 2007). There are also notable regional differences, that will be detailed further below. The comparison with observations has to be considered with caution because of significant observation errors. For instance, Kwok (2002), comparing PMW retrievals of ice concentration to equivalent synthetic aperture radar (SAR) inferences (with higher resolution, therefore more accurate), found that the PMW overestimates the winter open water coverage by 3–5 times. In summer, the observed PMW summer ice concentrations are subject to large uncertainties due to melt pond effects, reaching up to 15–20% in the Bootstrap data set.

Northern Hemisphere. In winter, first, the simulated NH ice concentrations (see Fig. 4) inside the pack are overestimated by a few percent. The observation error has the same order of magnitude.

Second, the simulated width and concentration of the ice stream along the east coast of Greenland is overestimated in winter, as in LIM1 and virtually all AOMIP models. Therefore, this must be due to the absence of specific atmospheric processes in the NCEP/NCAR reanalyses (e.g., katabatic winds) or to a common model feature (ice deformation field, absence of ocean waves and tides). Nevertheless, compared with LIM1, the ice-covered region in LIM3 is narrower and the ice pile-up in Denmark Strait disappears. This seems to be due to the introduction of the ITD, as in that location, the transition from VP to EVP minorly affects the results. In sea ice models with ITD, thin ice quickly disappears in the marginal ice zones during early summer, which leads to lower ice concentrations than in single-category models, promotes higher absorption of shortwave radiation in the ocean and intensifies the ice basal melt. This more realistic ice-albedo feedback was also found in the global climate model simulations of Holland et al. (2006). Here, only the ice–ocean part of this mechanism is active.
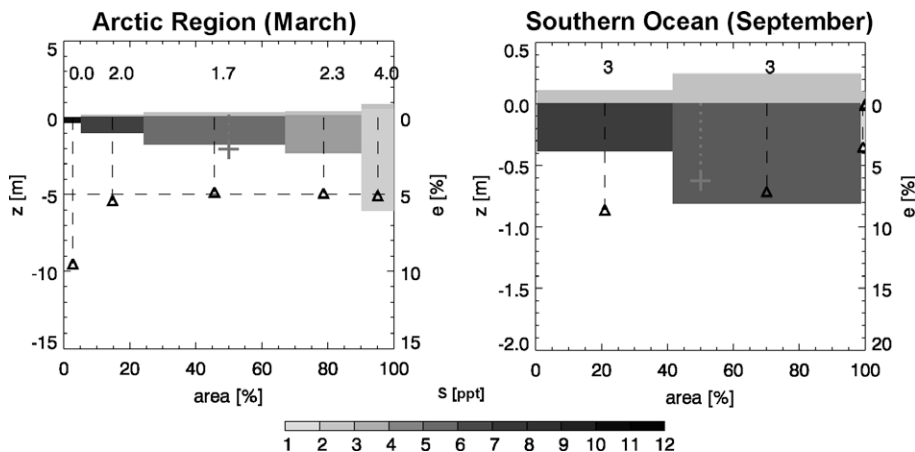

Fig. 2. Average winter sea ice physical state (1979–2006), for the Arctic regions (including the Arctic Ocean and the Beaufort, Chukchi, East Siberian, Laptev and Kara Seas) and the whole SH, detailed for each ice thickness category. The ice concentrations are represented horizontally. The ice thicknesses (negative values) and snow depths (positive values) are shown vertically (note the difference in scale between the two plots). The grey colors refer to the ice salinity. The black triangles indicate the relative brine volume e (computed from temperature and salinity), averaged over the vertical ice layers. The numbers on top are ice ages (years for the Arctic and months for the Antarctic). The cross indicates the mean ice thickness.

Table 4
Global sea ice statistics for the control simulation.

Variable (units)	Hem.	Mean	Av. max	Av. min	T_{mean} (U/decade)	T_{max}	T_{min}
Area (10^6 km^2)	N	10.2 ± 0.4	14.2 ± 0.3	4.4 ± 0.8	-0.32 ± 0.007	-0.18 ± 0.005	-0.62 ± 0.01
Thickness (cm)		191 ± 25	269 ± 38	141 ± 23	-25 ± 3	-34 ± 6	-22 ± 3
Velocity (cm/s)		4.5 ± 0.3	5.2 ± 0.6	3.3 ± 0.7	0.3 ± 0.06	0.003 ± 0.1	0.4 ± 0.2
Salinity (‰)		3.6 ± 0.2	4.6 ± 0.3	2.0 ± 0.01	0.2 ± 0.03	0.3 ± 0.04	0.005 ± 0.004
Age (years)		2.6 ± 0.3	4.0 ± 0.4	2.1 ± 0.4	-0.2 ± 0.07	-0.1 ± 0.09	-0.3 ± 0.07
Area (10^6 km^2)	S	11.8 ± 0.4	19.5 ± 0.5	0.9 ± 0.6	0.22 ± 0.006	0.22 ± 0.01	0.25 ± 0.01
Thickness (cm)		42 ± 1	58 ± 2	22 ± 4	0.6 ± 0.3	-0.5 ± 0.4	2.9 ± 0.7
Velocity (cm/s)		6.3 ± 0.2	8.6 ± 0.8	2.3 ± 0.4	0.09 ± 0.04	-0.01 ± 0.2	0.2 ± 0.007
Salinity (‰)		6.3 ± 0.1	9.1 ± 0.6	4.3 ± 0.5	-0.08 ± 0.01	-0.5 ± 0.1	0.3 ± 0.1
Age (years)		0.3 ± 0.03	0.9 ± 0.1	0.1 ± 0.04	0.03 ± 0.004	0.04 ± 0.03	0.04 ± 0.007

The means are successively computed over categories (weighed by the area of each category for the computation of area, velocity and age; by volume for thickness and salinity), then over the ice covered domain and finally over the 1979–2006 period.
Maxima and minima refer to the extremum values over the mean seasonal cycle.
The trends (T_{mean}, T_{max} and T_{min}) and the standard deviations are computed using the time series of the annual mean, minimum and maximum values.

Fig. 3. Mean seasonal cycles of NH and SH sea ice areas (black) and extents (grey) in the NEMO–LIM3 reference simulation (solid) and in observations derived from satellite Bootstrap PMW recordings (dashed; Comiso, 2007). Ice extent is the area enclosed in the 15% concentration contour, while ice area is the total area of ice.

and most AOMIP models, which underestimate (overestimate) the ice concentration in the central Arctic (in the Siberian seas). Over the three AOMIP models including an ITD, two of them show a similar, realistic latitudinal decrease in ice concentration.[8] Yet this latitudinal decrease is not sharp enough in LIM3. LIM3, as LIM1 and more than half of the AOMIP models, including the most realistic ones, does not reproduce the observed summer ice retreat in the Laptev and East Siberian Seas. This suggests that the ice models miss or misrepresent some important processes in the shelf regions (e.g., tides, river runoff, ...). In addition, the ice retreats too far in the Northeastern Kara Sea, and the ice concentration is underestimated in the Atlantic sector of the Arctic Ocean (i.e., between Spitsbergen, the North Pole and Severnaya Zemlya). This is associated with an underestimation of ice thickness in those areas (see Section 4.3.1) and is consistent with the fact that there is a 1–2 °C warm bias in the NCEP temperatures in summer (see, e.g., Hunke and Holland, 2007). Finally, ice unrealistically subsists in summer in the Northern Baffin and Hudson Bays, as in LIM1 and in some AOMIP models. In those regions, there are numerous mesoscale features which cannot be resolved by our model.

Southern Hemisphere. In the SH, as in LIM1, the location of the simulated winter ice edge is slightly too far northward off East Antarctica and in the Amundsen and Bellingshausen Seas (see Fig. 5). In contrast to this, the winter ice extent is slightly underestimated in the Weddell and Ross Seas. Northward, the ice extent is limited by the westerly winds and the position of the Antarctic Circumpolar Current (ACC) which, even in winter, has surface temperatures above the freezing point and acts as a permanent heat source. Its course is largely determined by bottom topography which, especially in a *z*-coordinate model at 2° mean resolution, does not necessarily capture all details of the real bathymetry.

The simulated winter ice concentrations are overall overestimated in the SH. In addition, the width of the marginal ice zone is underestimated. This differs from LIM1. In LIM1, the high h^0 prevents the fast closure of open water and regulates the fall advance of the ice edge. We will come back to this problem in Section 4.3.1.

In summer, the simulated sea ice distribution shows a lack of sea ice near the tip of the Antarctic Peninsula and along the coast of East Antarctica. Following Timmermann et al. (2005), we attribute the first mainly to a poor representation of the Antarctic Peninsula in the atmospheric forcing fields and the latter to the model's relatively coarse resolution and inability to simulate the landfast ice along Antarctica, especially between 90° and 180 °E. Indeed, the observed width of the landfast ice band is on average 45-65 km but can reach 270 km in some regions, as pointed out

In addition, as in LIM1, the Odden/Nordbukta structure is absent in NEMO–LIM3. The Odden ice tongue is located in the Greenland Sea and covers over all or part of the area of influence of the Jan Mayen Current and that encloses a bay of open water called Nordbukta. Variability of the ice tongue is strong at scales from daily to interdecadal (Comiso et al., 2001). The absence of the Odden feature is due to the relatively low model resolution and appears in OPA9-LIM2 with grid resolution finer than 0.5° (Drakkar Group, personal communication). At 2°, the Odden would only cover 3–4 grid cells in zonal extent, so that none of the hypothesized mechanisms for Odden ice formation (e.g., cold air outbursts, instabilities of the East Greenland Current) is covered in enough detail. This is also supported by AOMIP results, which indicate that models with sufficient spatial resolution and at least VP dynamics[7] manage to capture the Odden ice tongue.

In summer, the simulated geographical distribution of ice concentration features high values in the central Arctic and a sharp decrease toward lower latitudes. This is more realistic than in LIM1

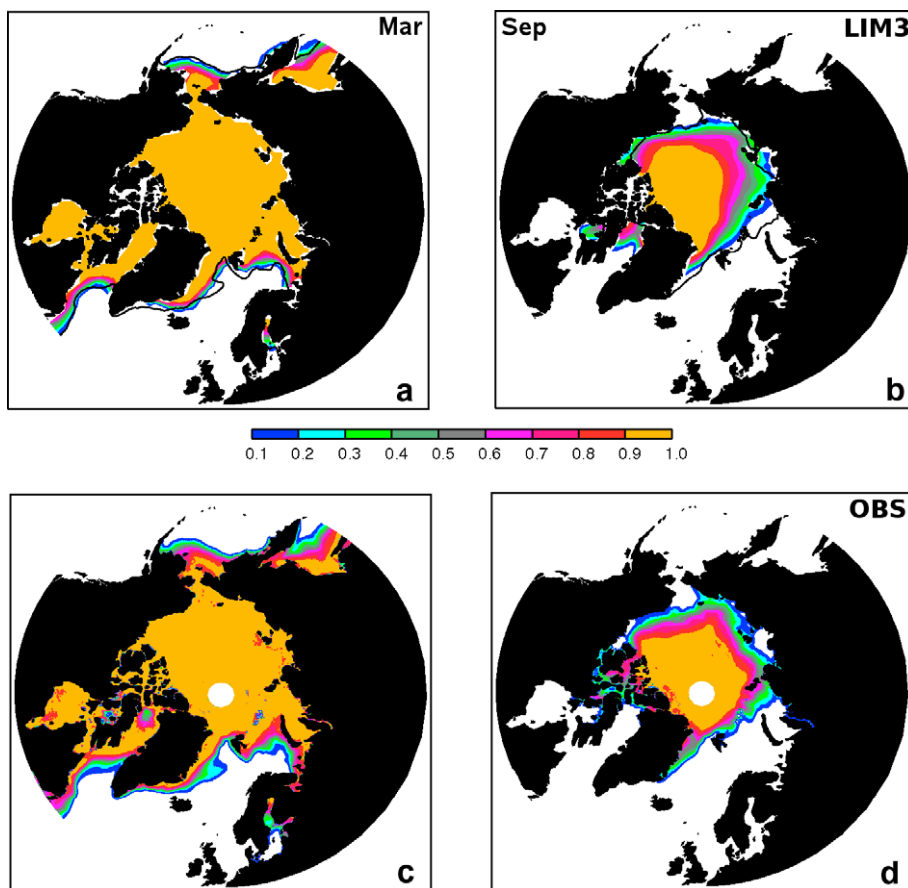[7] e.g., the UW and NPS models.

[8] The LANL and RAS models.

Fig. 4. Simulated March and September geographical distributions of mean NH (a and b) ice concentration (1979–2004), indicating the extrema of ice coverage. The observed mean ice edge (solid grey lines) derived from the PMW Bootstrap dataset (Comiso, 2007) is also depicted. The corresponding observed PMW ice concentration data, for the same period and regions, are shown in panels (c and d).

by Russian long-term monitoring in the second half of the 20th century (Fedotov et al., 1998).

4.2.3. Interannual variations

Regarding the model annual mean ice extent, for the 1979–2006 period, we find, in the NH, a linear trend of $-0.32 \pm 0.007 \times 10^6$ km^2/decade (obs. $-0.40 \pm 0.02 \times 10^6$ km^2/decade; Comiso and Nishio, 2008). In the SH, there is a simulated increasing trend of $0.22 \pm 0.006 \times 10^6$ km^2/decade (obs. $0.11 \pm 0.02 \times 10^6$ km^2/decade). Trends for minimal extent are the largest in both hemispheres. See Table 4 for more information.

Time series of monthly mean anomalies of NH ice area (i.e., differences of monthly means from the mean seasonal cycle, Fig. 6) are well represented by the model (correlation with obs. = 0.74). The simulated anomalies of ice area feature, first, an increase until 1988, then a series of alternating maxima and minima and, finally, a gradual decrease until 2006. In the 2000s, the model simulates the observed series of pronounced minima of area (Stroeve et al., 2005). The typical geographical distribution of the simulated concentration anomalies in the 2000s frequently shows negative concentration anomalies located near the centre of the Siberian shelf, while in observations they are found rather in the East Siberian, Chukchi and Beaufort Seas (see Fig. 7b–d).

Some years are not well simulated. First, in 1981, the NCEP/NCAR winter air temperatures are higher than observations from the Russian meteorological stations located on the Siberian coast (Tartinville et al., unpublished manuscript). Spurious minimum of NH ice extent is simulated accordingly. Second, in the 1980s, the model overestimates ice extent. Finally, in the 1990s, the model overestimates ice extent at the time of the 1993 and 1995 minima. Spatial distributions of concentration anomalies (see Fig. 7a and c) show that the observed retreat is not strong enough on the Siberian shelf.

In the SH, the simulated interannual variations are larger than in the Arctic and generally well captured by the model (correlation with obs. 0.65). In winter, the geographical distribution of ice concentration anomalies is usually correct, though their amplitude is typically underestimated, presumably because atmosphere-ice/ocean feedbacks are not included in the model. In summer, the location of anomalies is correct, except where the ice retreats too far in the model (e.g., in the central Weddell Sea in 1986, see Fig. 8). In particular, in 2001, the simulated ice retreat is too slow. This triggers a strong discrepancy between model results and observations.

4.3. Ice thickness and volume

4.3.1. Ice thickness

The model 1979–2006 NH (SH) mean ice thickness equals 1.91 ± 0.25 (0.42 ± 0.01) m. In the NH, the interannual variability in ice thickness (standard deviation equals 12% of the mean) is higher than for ice area (3%). In the SH, the ice thickness variability is not as high (4%).

Northern Hemisphere. The simulated winter sea ice thickness features a gradient of ice thickness from 0–2 m on the west Siberian shelf to 3.5 m at the North Pole and a 5–6 m maximum off Greenland and Canada (see Fig. 9), while ice is consistently thin (0–1.5 m) in the seasonal ice zone. Qualitative comparison to the
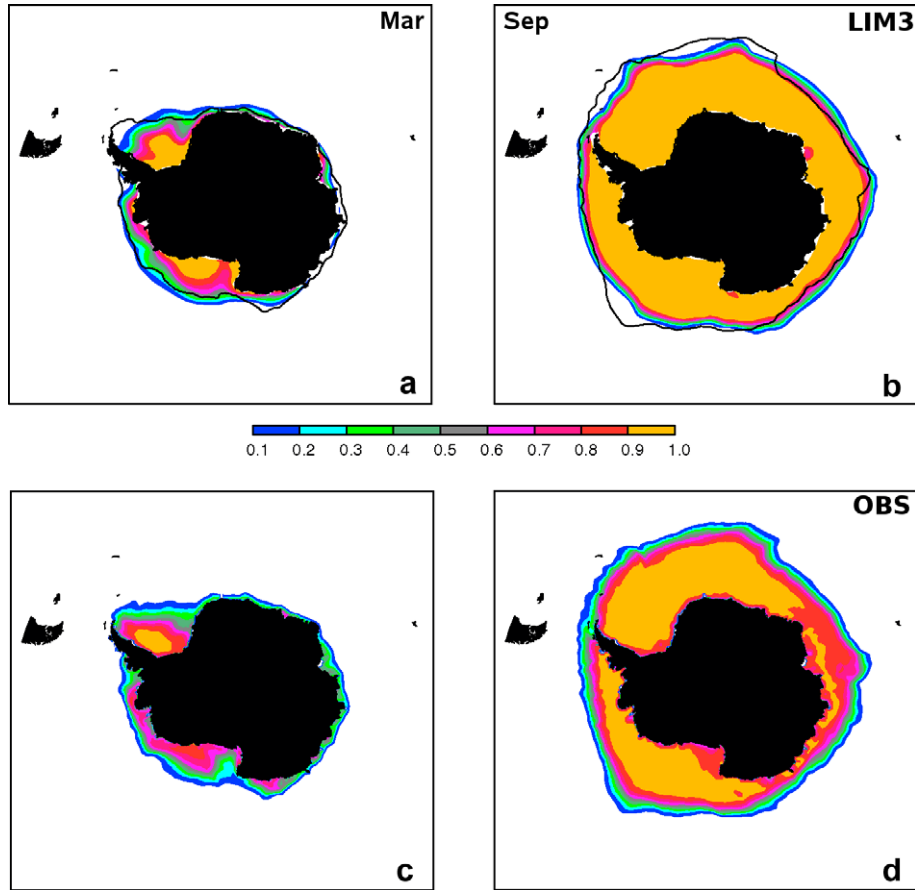
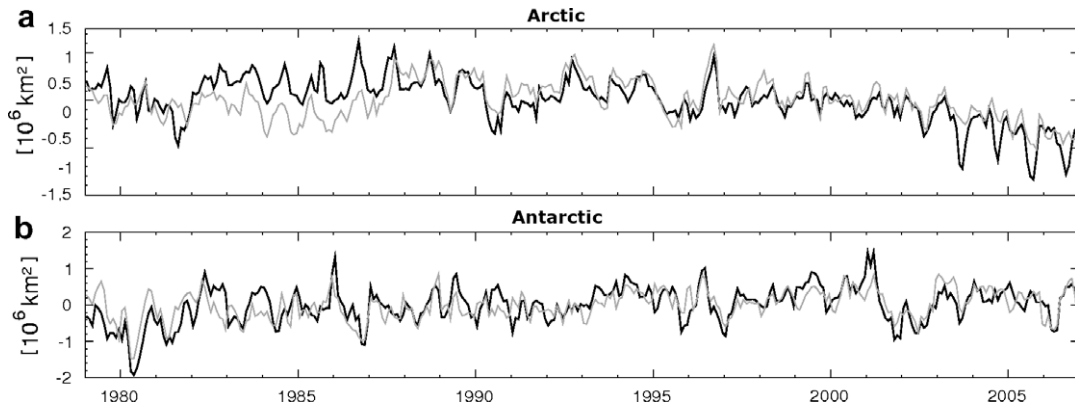**Fig. 5.** Same as Fig. 4, but for the SH.

Fig. 6. Time series of monthly mean anomalies of sea ice area for the NH (a) and SH (b) as simulated by the model (black) and in observations derived from satellite PMW recordings (grey; Comiso, 2007).

October–March 1993–2001 ice thickness data derived from satellite altimetry (Laxon et al., 2003) also shows good agreement. The largest model–data differences (estimated visually) are negative and located in the Northern Barents Sea ($\Delta = -1.5$ m) and along the east coast of Greenland ($\Delta = -2$ to -3 m). They indicate an underestimation of the volume of ice exported out of the Arctic Ocean through Fram Strait and Barents Sea.

Quantitative comparison of model values to the submarine ULS ice drafts at the same time and location (Rothrock et al., 2003; see Fig. 9b) confirms and refines the aforementioned underestimation. Observed ice drafts, averaged over 3478 50 km-long transects from 37 cruises spanning the years 1975–2000, are used. Observed ice

drafts are converted into thicknesses using the snow depth climatology of Warren et al. (1999). The results indicate an average model underestimation of ice thickness ($\Delta = -0.55 \pm 1.04$ m). First, the temporal evolution of the annual mean model-ULS difference shows no trend over the years. Most of the years, the absolute error is small and comprised between -0.8 and 0.2 m (average -0.41 m). From 1981 to 1983, the model error is larger (from -0.88 to -2.22 m) because of the error in the NCEP/NCAR temperatures (see Section 4.2.3). In 1989 and 1998, the model underestimation is also larger ($\Delta = -1.5$ m), in particular close to the North Pole. Second, averaged on a monthly basis, independently of the year of observation and looking at the seasonal perspective, the
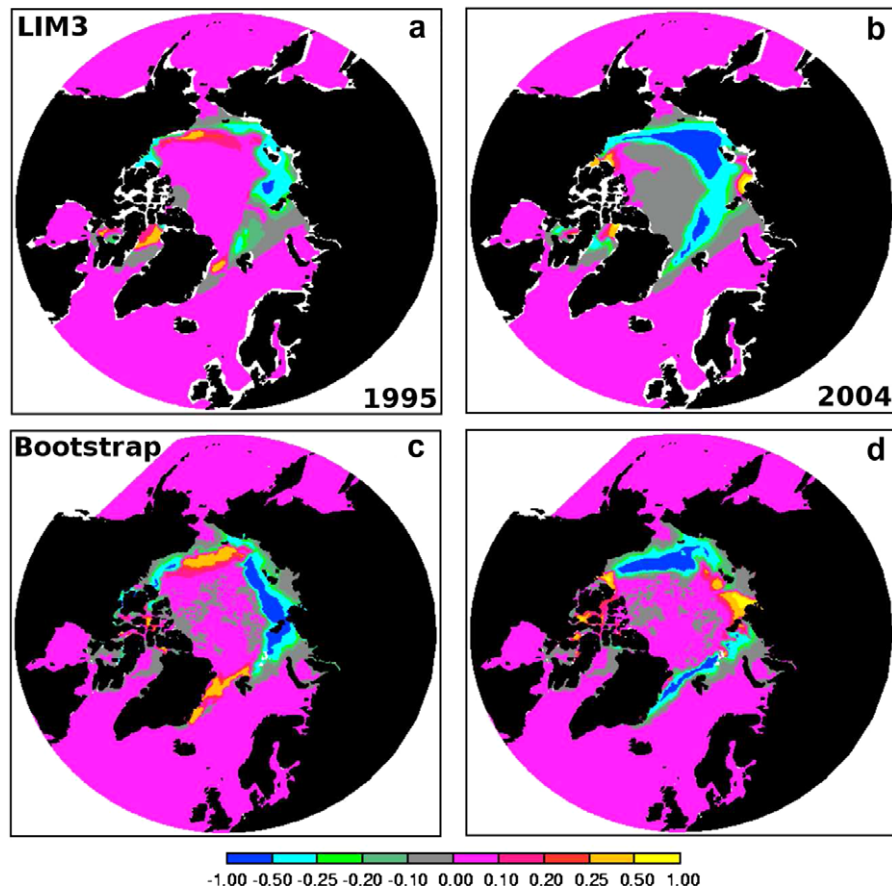
Fig. 7. Simulated September ice concentration anomalies for two years in the NH (1995, a; 2004, b). (c–d) Same, but for PMW Bootstrap observations (Comiso, 2007). Anomalies are computed using 1979–2004 as the reference period.

model-ULS difference is clearly larger in summer ($\Delta = -1.54$ m in September) than in winter ($\Delta = -0.06$ m in April–May). Finally, the geographical distribution of the model-ULS differences shows large negative values in the Beaufort Gyre and large negative values in the Atlantic sector of the Arctic Ocean between Spitzbergen and the North Pole. This pattern is stable over the years and is remarkably similar to results of simulations performed with other multi-thickness sea ice models (see Rothrock et al., 2003, Fig. 9; Wilchinsky et al., 2006, Fig. 7; Bitz et al., 2001, Fig. 9). Therefore, it must be due to a common model feature. The error magnitude, typically comprised between −2 and 2 m and also consistent over the different models suggests that the origin of the error lies in the model dynamic component. Wilchinsky et al. (2006) proposed a modification of the yield curve which takes sliding friction into account and reduces model error.

Compared to LIM1, LIM3 has a more realistic geographical distribution of ice thickness. The Siberia–Canada thickness gradient is larger. Ice is thinner in the Barents, Kara and Laptev Seas ($\Delta h_{LIM3-LIM1} = -1$ m), in the East Siberian Sea ($\Delta = -0.5$ m) and in the Beaufort and Chukchi Seas ($\Delta = -1$ m). This is due, first, to the lower h^0, which promotes thinner new ice and, second, to the more intense summer melt induced by the stronger ITD-associated ice-albedo feedback. In addition, ice is thicker along the Canadian Coast ($\Delta = 0$–1.5 m).

Southern Hemisphere. The simulated geographical sea ice thickness distribution in the SH has typical values ranging from 0.5 to 1 m, increasing southwards, with a local maximum of 1.5 m in the Ross Sea. Along the coast of East Antarctica and in the Ross Sea, the model features a series of polynyas locally reducing ice thickness.

In the SH, the data are even more sparse than in the Arctic. The only ice thickness dataset in the Southern Ocean is provided by the ASPeCt group (Antarctic Sea ice Processes and Climate, see Worby et al., 2008), which is a compilation of visual ship-based observations of ice thickness, covering almost all the Southern Ocean but with some potential biases due to preferential ship track crossing thin ice and to varying date of observation. Comparison of model results to the ASPeCt dataset shows reasonable agreement, though model ice thickness is underestimated. The typical simulated first year (FY) ice thickness is underestimated by 0–0.5 m. In older ice areas, the ice thickness is further underestimated: along the east coast of the Antarctic Peninsula (1.5 m), along the west Pacific coast of Antarctica (0.5 m) and in the Amundsen and Ross Seas (0.5–1.5 m).

Now, we discuss the circumpolar low bias in ice thickness in the SH. Simulated winter ice concentration is higher than observed, in relation with missing dynamical processes in the model (tides, inertial oscillations, waves) that would enhance open water production, heat loss and, in turn, ice production in open water. In LIM1, In order to solve this issue, h^0 was raised to 1 m, which reduces the area of newly formed ice, maintains relatively large winter open water area and sustains new ice production. For similar reasons, using an artificially high value of $h^0 = 1$ m in the multi-category framework of LIM3 results in thicker sea ice in the SH. However, it also strongly deteriorates the Arctic. For consistency between the two hemispheres, we therefore keep the simulated value of h^0 which is close to 10 cm in LIM3. As a result, all over the SH, sea ice is thinner and more concentrated in LIM3 compared with LIM1. Furthermore, as the ice is too thin by the end of the winter, it also disappears faster in summer, which prevents the
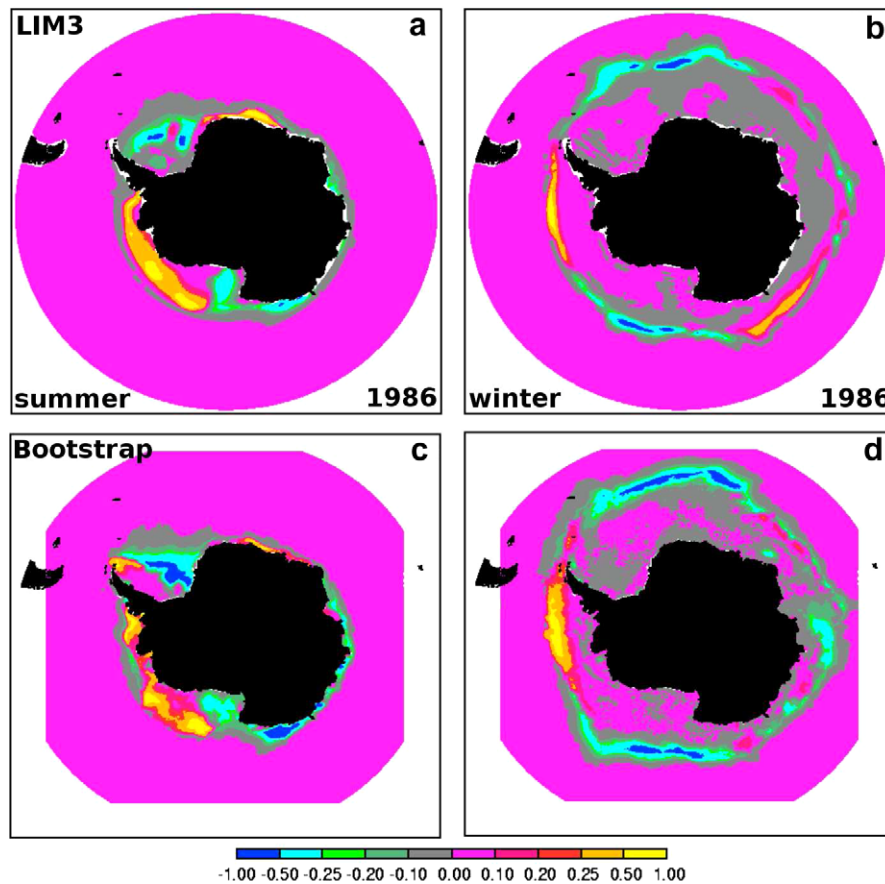
Fig. 8. Simulated September ice concentration anomalies for September (a) and March (b) 1986 in the SH. (c and d) Same, but for PMW Bootstrap observations (Comiso, 2007). Anomalies are computed using 1979–2004 as the reference period.

maintenance of a thick MY ice cover in coastal areas. Finally, east of the Antarctic Peninsula, following Timmermann et al. (2005), we argue that the negative bias in ice thickness is due to the underestimation of deformed ice production, caused by poor representation of the winds in the forcing data as well as by the absence of tides in the model. In addition, there is excessive melting due to a warm bias in the forcing data.

4.3.2. Ice volume

The ice volume is the domain integral of the product of ice thickness by ice area. In the NH, on average, the simulated ice volume has its maximum at 25×10^3 km^3 in early April and reaches its minimum in mid-August at 11.8×10^3 km^3, which lies in the range of the different available simulations over the same period (see, e.g., Rothrock et al., 2003; Gerdes and Köberle, 2007). Interannual variations are significant. First, from 1979 to 1982, an initial decrease in annual mean NH ice volume (-2.03×10^3 km^3/y) is simulated. Nevertheless, the latter may well be not realistic since the NCEP/NCAR air temperatures are warmer than observed during that period (see Section 4.2.3). Then, from 1983 to 1987, the simulated NH annual mean volume increases at a rate of 1.04×10^3 km^3/year, reaching 29.4×10^3 km^3 in 1989. Finally, from 1988 to 2006, the NH annual mean volume decreases at a rate of -0.46×10^3 km^3/year. In the SH, the ice volume on average reaches its maximum in early September at 8.8×10^3 km^3 and then decreases to 300 km^3 by the end of January. The annual SH ice volume shows no trend.

4.3.3. Sea ice mass balance

Northern Hemisphere. The different components of the simulated sea ice mass balance differ from one hemisphere to the other

(see Fig. 10). In the Arctic Region (see the caption of Fig. 2 for a definition), averaged over the 1979–2006 period, annual freezing at the ice base contributes by 89% to the total annual growth. New ice formation in open water only contributes slightly (10%), while snow ice formation is negligible (0.1%). Analyzing the structure of ice cores extracted from ice exiting the Arctic basin through Fram Strait Tucker et al. (1987) found 90% of columnar ice (indicating basal congelation process), in agreement with our simulations. Simulated annual basal melt contributes by 59% to the total, which is slightly higher than surface melt (41%), especially due to the thinner ice categories. This is comparable to the SHEBA[9] station observations, where roughly equivalent contributions from basal and surface melt were observed (Perovich et al., 2003).

Southern Hemisphere. In the SH, the simulated basal congelation is important (37% of the annual volume created). Nevertheless, in contrast to the Arctic, new ice formation in open water (38%, mostly in fall) and snow ice formation (25%, mostly in spring) have a significant impact on the sea ice mass budget. Ice core structural analyses by Jeffries et al. (1997) and Worby et al. (1998), performed in situ in the Ross and Amundsen Seas and along the coast of East Antarctica, respectively, found 26% (resp. 39%) of columnar ice, 44% (resp. 47%) of granular ice – which indicates frazil ice formation in turbulent waters – and 24% (resp. 13%) of granular ice with snow ice origin. This suggests that our model probably overestimates the ratio of basal ice growth to frazil ice formation in the Southern Ocean. As a consequence of the large simulated oceanic

---

[9] SHEBA (Surface Heat Budget of the Arctic Ocean) was a yearlong drift station in the Beaufort Sea between October 1997 and September 1998.
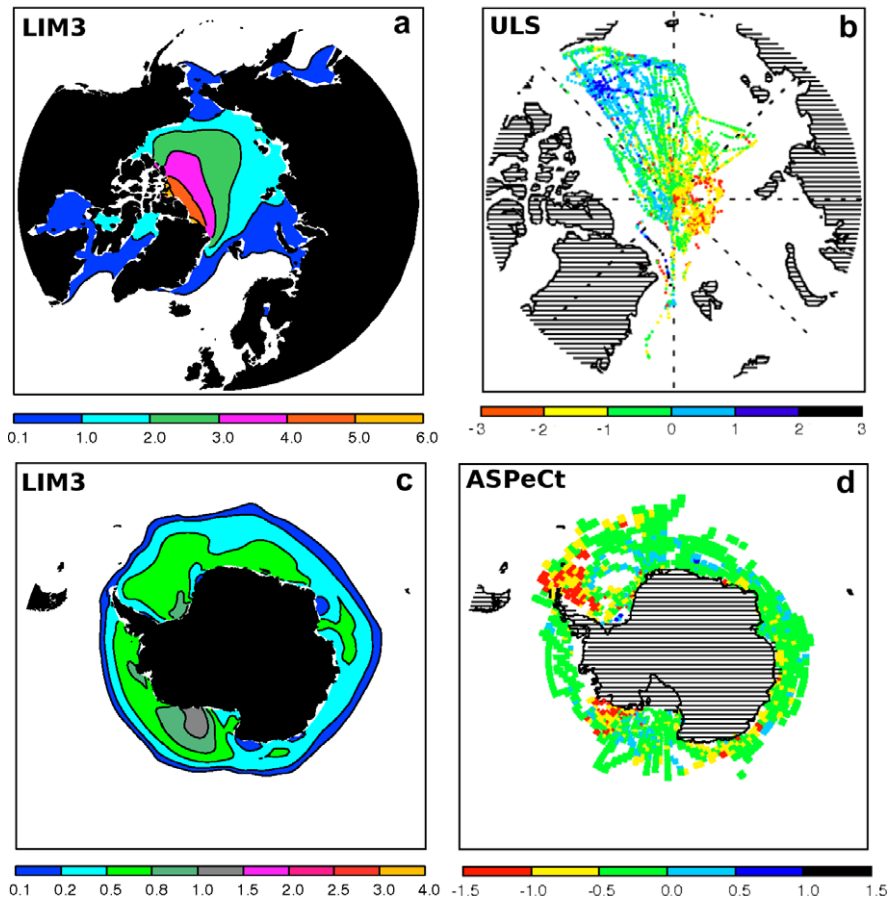
Fig. 9. Simulated geographical distribution of ice thickness (m) in the NH (January, a) and SH (September, c). On plate (b), the differences between model and ULS data in the NH are shown. The differences are computed using ULS draft values averaged over 3478 transects spanning 37 submarine cruises between years 1975 and 2000 (Rothrock et al., 2003). Drafts are converted into thicknesses using the snow depth climatology of Warren et al. (1999). Each ULS thickness is compared with the monthly mean model value which year, month and grid coordinates are chosen as the closest to the actual ULS observation. Since ULS averages include open water, the model mean ice thickness used accounts also for open water fraction. In plate (d), the differences between model and ship-based ASPeCt observation dataset (Worby et al., 2008) are shown. The differences are computed first, by gridding the ASPeCt observations to the ORCA2 grid, then, by computing the average months of observation and, finally, by comparing the resulting value to a monthly mean 1979–2006 model value which month and grid coordinates are chosen as the closest to the corresponding ASPeCt observation.
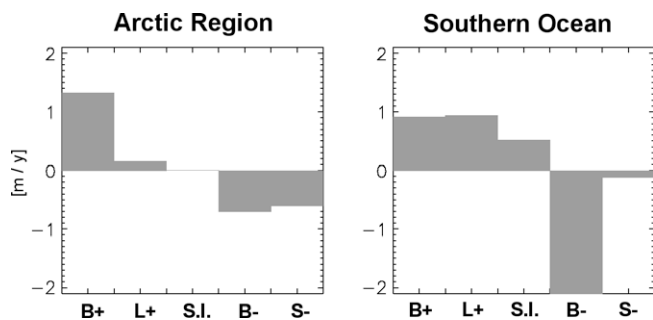
Fig. 10. Annual 1979–2006 averages of source/sink terms of ice volume per unit area due to different mechanisms: basal growth (B+), new ice growth in open water (L+), snow ice formation (S.I.), basal melt (B−) and surface melt (S−) for the Arctic region (left, see caption of Fig. 2 for a definition) and the whole Southern Ocean (right).

heat flux (10–40 W/m^2), basal melt tremendously dominates the decay of the ice cover (95% of the total), while surface melt is practically absent, which corresponds to available observations (Andreas and Ackley, 1982; McPhee et al., 1998).

The underestimation of frazil ice production in open water confirms that the SH dynamic processes of ice growth are not accurately represented in the model. In the SH, new ice is known to grow in wavy, turbulent waters, in what is called the pancake cycle

(Lange et al., 1989). During this process, significant open water areas are created and destroyed at very short time scales by wave–ice interactions.

4.3.4. Ice thickness distribution

We compare here the simulated ITD with four sets of observed ITD from both hemispheres (see Fig. 11a–d). Observations come from different sources and techniques: (1) Witte and Fahrbach (2005), moored ULS in the Fram Strait region; (2) Haas (2004), electromagnetic sounding and drilling in the Transpolar Drift region; (3) Worby et al. (1996), drilling and ship observations in the Amundsen and Bellingshausen Seas; (c) Lange and Eicken (1991), drilling in the Northwestern Weddell Sea.

The simulated ice thickness distribution follows the commonly observed features. NH ITD is a mixture of level FY and MY ice as well as thick ridged ice. In relation to the mean ice thickness underestimation discussed earlier, the model ITD features an excess of thin ice and a lack of thick ice. In the SH, the most representative ice type is level FY ice. Nevertheless, the simulated SH ITD has a lack of thick MY and ridged ice.

The interannual variations in NH annual mean ITD (panel e) are quite significant. In the 1980s, until 1987, the modal thickness as well as the relative contribution of thick categories increase. In 1988, the coverage of the thickest ice decreases and, in 1989, the modal ice thickness also starts to decrease, which, as pointed out
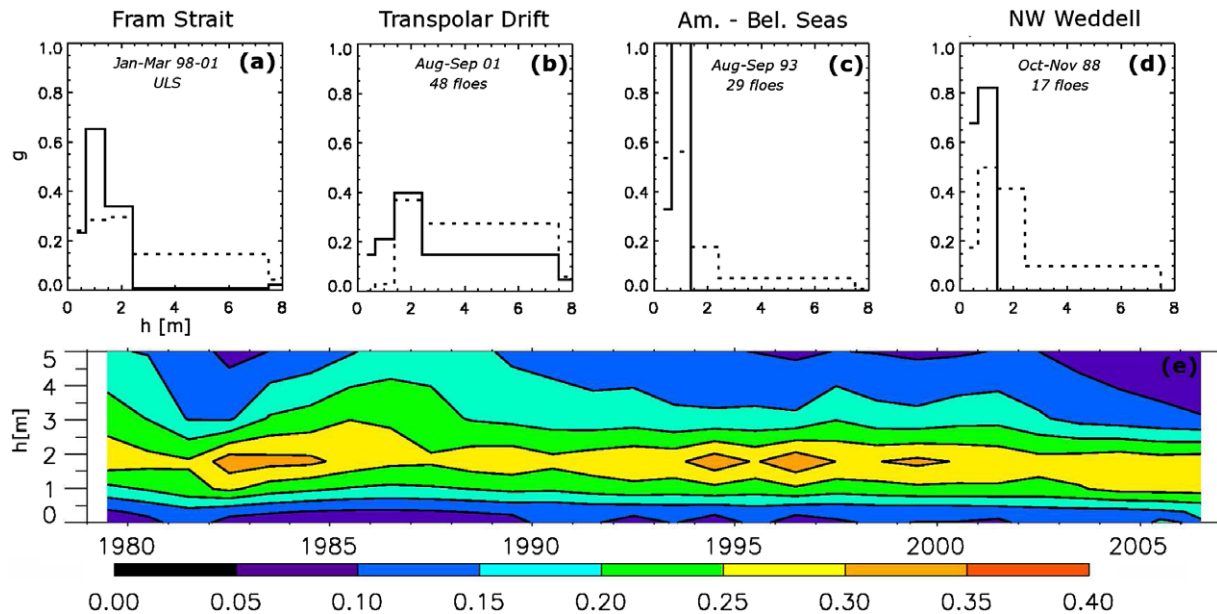
Fig. 11. (a–d) Comparison of simulated (solid) and observed in situ (dashed) ITD, excluding open water. Observations come from (a) Witte and Fahrbach (2005), moored ULS; (b) Haas (2004), electromagnetic sounding and drilling; (c) Worby et al. (1996), drilling and ship observations and (d) Lange and Eicken (1991), drilling. The simulated distribution is a 2-month mean taken from the closest grid point at the corresponding time of the year. (e) Simulated Arctic (including Arctic Ocean, Beaufort, Chukchi and all Siberian shelf seas) annual mean ice thickness distribution, including open water, 1979–2006 (contours).

by several authors (see, e.g., Lindsay and Zhang, 2005), was triggered by a switch towards positive Arctic Oscillation (AO) index, also called the Northern Annular Mode. Defined as the first leading EOF of sea-level pressure (SLP) above 60°N, the AO is the dominant pattern of non-seasonal SLP variations in the Arctic. AO changes are thus associated with a clear modification of the wind forcing and, in turn, of the large-scale ice motion in the Arctic basin (Rigor et al., 2002). Weaker (stronger) Beaufort Gyre and higher (lower) than normal values of ice export through Fram Strait are associated with high (low) values of the AO index, and result in low (high) sea ice coverage over the Siberian shelf seas. Higher AO index in the 1990s resulted in an increase in the flushing of old, thick ice out of the Arctic Basin through Fram Strait. From 1996 on, the AO index recovered back to more normal values but the thinning continued. As hypothesized by Lindsay and Zhang (2005), the Arctic sea ice cover seems to have reached a tipping point.

4.4. Ice drift

4.4.1. Drift patterns

The large-scale simulated sea ice drift reflects the general patterns of atmospheric circulation. Ice motion is more intense in the SH, due to higher winds and lower continental constrains. The 1979–2006 average simulated ice velocity for the NH (SH) is 4.5 (6.3) cm/s, which corresponds well to satellite observations of ice motion. The standard deviation is higher in the NH (34% of the mean) than in the SH (19%). From 1979 to 1986, the NH simulated ice velocity decreases by 0.8 cm/s per decade, and then increases until 2006 at a rate of 0.5 cm/s per decade. No remarkable evolution is found in the SH.

The drift patterns are very similar to those shown by Timmermann et al. (2005) and Bouillon et al., (2009) (using LIM1 with VP and EVP, respectively) and compare quite well to the observations of Fowler (2003). In the NH, the mean ice drift field shows the divergent motion over the Siberian shelf (1–2 cm/s), the Beaufort Gyre (1–3 cm/s), the Transpolar Drift Stream (1–4 cm/s), the more rapid ice current across Fram Strait (4–8 cm/s) and along the east coast of Greenland (5–10 cm/s), as well as a large nearly

motionless ice zone north of Greenland and the Canadian Archipelago.

In the SH, the model drift features the coastal (3–13 cm/s) and offshore circumpolar (1–6 cm/s) currents, as well as the Weddell and Ross Gyres. Spurious maxima of ice velocity are found along the coastal areas of the Indian (4–10 cm/s) and west Pacific (5–10 cm/s) sectors of the Southern Ocean, as well as in the Western Ross Sea (5–10 cm/s), where satellite observations show that ice is almost at rest, which is supported by in situ observation of large bands of landfast ice in the west Pacific sector (Fedotov et al., 1998). The position of the transition zone between coastal and offshore currents is well captured between 67° and 72°S. A more quantitative analysis of sea ice drift is done in Bouillon et al., (2009).

4.4.2. Fram Strait export

Fram Strait, situated between Greenland and Svalbard, is the main output gate for sea ice out of the Arctic Ocean and has therefore an important impact on the NH ice volume. The simulated annual areal export through Fram Strait is 0.9×10^6 km², i.e., 12% of the Arctic Ocean area, which compares well to the data of Kwok et al. (2004) and the 13% in the Lindsay and Zhang (2005) simulation (Fig. 12). The seasonal variations (with high winter and low summer exports) also follow the observations. The area flux has no significant trend over the simulation.

In LIM3, the simulated annual mean sea ice volume export flux through Fram Strait is 1.2×10^3 km³ which underestimate by 45% the observed value of Kwok et al. (2004), derived through a combination of radar and ULS data. The exported ice (i.e., ice from the Atlantic sector of the Arctic Ocean) is therefore too thin in the model, which is coherent with the analysis of the ice thickness fields in the Atlantic Sector of the Arctic Ocean. As in Lindsay and Zhang (2005), the winter volume flux has maxima in 1989 and 1990, which is caused more by the large mean thickness than by a large area flux. The winter sea ice volume flux declines in the late 1990s because the mean exported thickness declines.

LIM1 overestimates sea ice thickness by around 2 m in the NH. Consequently, the annual Fram Strait sea ice volume export in LIM1 is 3.5×10^3 km³, i.e., 60% larger than observed and almost

Fram strait areal export
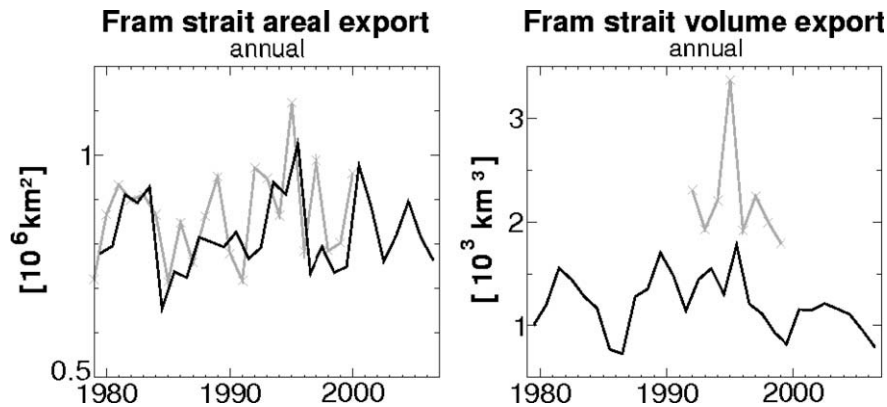annual

Fram strait volume export
annual

Fig. 12. Simulated (black) and observed (grey) time series of annual mean sea ice areal (left) and volume (right) exports through Fram Strait. Observations combine recordings from synthetic aperture radar and moored ULS data (Kwok et al., 2004).

three times larger than in LIM3. This has important consequences on the oceanic circulation (see also Section 3.3). As shown in Vancoppenolle (2008), the simulated mean meridional overturning stream function in the North Atlantic is 18 Sv in NEMO–LIM3, which is 10 Sv higher compared with NEMO–LIM1. The THC is controlled by deep convection in the Northern North Atlantic. In that location, the dilution role of sea ice inflow has a strong influence on the buoyancy forcing, which controls deep convection and, in turn, the strength of the THC. In NEMO–LIM3, due to the reduced ice volume export through Fram Strait and freshwater transport to the North Atlantic, the surface waters are 0–0.5‰ more saline south of Greenland compared with NEMO–LIM1. Consequently, the geographical distribution of the convection sites in the North Atlantic is much better simulated in NEMO–LIM3 compared to NEMO–LIM1, with differences in mixed layer depth between the two models up to 2000 m in the Labrador Sea.

4.5. Snow volume and depth

In spite of its important impact on the surface heat fluxes (Fichefet et al., 2000), the mass of snow on sea ice and its interannual variations are not well known, and this for several reasons. First, large-scale observations of snow depth are recent and the knowledge of the sources of error is not yet optimal. Second, observations of snowfall are extremely difficult to carry out accurately. In particular, precipitation gauges underestimate snowfall significantly through wind undercatch, wetting and evaporation losses (Goodison et al., 1998). In addition, the link between precipitation and snow depth is not yet understood. In particular, the role of wind on snow resuspension and deposition on an ice cover of variable thickness is poorly documented and therefore neglected in models (Massom et al., 2001).

Northern Hemisphere. Averaged over 1979–2006, the simulated NH snow volume peaks at 2.8×10^3 km³ in early April and vanishes in mid-July. The simulated winter snow depth is around 30 cm in the Central Arctic, which corresponds to the climatology of Warren et al. (1999) derived from observations made at the Russian drift stations over 1954–1991. In the Arctic, unfortunately, no satellite record of snow depth exists, because the snow microwave signal is not discriminable from the one of MY ice (Markus and Cavalieri, 1998).

Southern Hemisphere. In the SH, algorithms allowing snow depth retrieval from PMW recordings have been developed (Markus and Cavalieri, 1998, 2006), though their level of validation is not as high as for ice concentration and the magnitude of errors is not well known. Averaged over 1979–2006, the model (observed) snow volume ranges from 0.12 (0.62) $\times 10^3$ km³ in early February

to 2.65 (2.34) $\times 10^3$ km³ in early September. In winter, the simulated maximum snow volume occurs 1 month later than observed.

Attributing errors would require an extensive study. The small winter overestimation may be linked to the absence of the model representation of snow metamorphism, in particular compaction (Sturm et al., 2002), or blowing snow and blowing snow sublimation effects (Déry and Tremblay, 2004), or both. It can also be linked to the precipitation forcing, which is poorly constrained by observations. The summer underestimation has to be interpreted with even more caution since data are subject to more errors during that season. First, the underestimation of ice concentration induces a smaller surface for snow. Second, this underestimation is consistent with the fact that 1-D models including a representation of snow cover similar to LIM3 prove to melt snow too quickly. As pointed out by 1-D studies (Nicolaus et al., 2006; VBF07), improving the model snow physics (e.g., snow metamorphism, radiative effects and thermodynamics) would likely give a slower snowmelt.

The geographical distribution (Fig. 13) of snow depth compares quite well with observations. The negative northward gradient and the regional accumulations (i.e., the maxima in the Weddell, Amundsen and Bellingshausen Seas, and the minimum in the Ross Sea) are well simulated. The lack of accuracy in the exact location of the maxima and in their amplitude probably reflects (1) the underestimated MY ice cover along the Antarctic Peninsula in the model (see Section 4.3.1), (2) the absence of redistributing wind effects and (3) errors in the forcing. Note that in the Eastern Ross Sea, the ASPeCt visual snow depth data set (Worby et al., 2008) also features a snow depth maximum between 0.4 and 0.6 m, while it is not so strong in the PMW dataset.

4.6. Sea ice age

4.6.1. Hemispheric mean values and interannual variations

Fig. 14 (panel a) shows time series and geographical distributions (panels b-c) of the simulated mean ice age (i.e., averaged over categories) in both hemispheres. Ice is older in the NH (average 2.6 years) than in the SH (0.3 years), which well represents the higher prevalence of MY in the NH (Cavalieri et al., 1997; Kwok, 2004). The mean seasonal cycle of ice age is characterized by a peak-to-trough amplitude equal to 1.91 (0.84) year in the NH (SH). The summer maximum, reached on Aug 23 (Feb 18) in the NH (SH), reflects the higher concentration of old ice. The time of the minimum, Feb 27 (Apr 14) in the NH (SH), reflects the time of the highest coverage of new ice.

Due to the sea ice age definition, the interannual variations in sea ice age mostly reflect the variations in ice area. The correlation
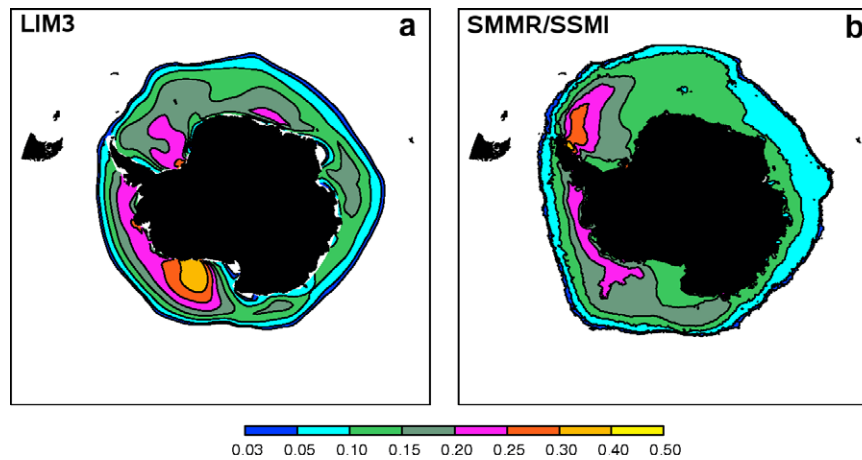
Fig. 13. Simulated (a) and observed (b) geographical distributions (September) of mean snow depth (m) in the SH. Observations are derived from satellite passive microwave recordings (Markus and Cavalieri, 2006). The means, computed over 1979–2004, take into account the weighed contributions of the ice thickness categories, but exclude open water.

between mean ice age and total ice area is 0.72 (0.58) in the NH (SH), but it is only −0.26 (−0.39) for ice volume. The NH sea ice age increases during the 1980s until 1989, remains stable until 1995, and then decreases monotonically, as also shown by observation-based computations of Rigor and Wallace (2004). The trend in ice age over the 1979–2006 period is significant in the NH with −0.18 year/decade. The decrease is more pronounced for the annual minimum, which indicates an increasing winter contribution of young ice to the overall ice pack. No such trend is found in the SH.

4.6.2. Geographical distribution

Northern Hemisphere. In the NH, the simulated geographical distribution of ice age features FY ice (0–1 year) in the Hudson and Baffin Bays and in the East Greenland, Barents, Kara, Chukchi and Okhotsk Seas. The intermediate ages (1–3 year) that are found in Laptev and Beaufort Seas, as well as in the Eurasian basin of the Arctic Ocean, reflect a mixture of young, thin, FY ice and old, thick, MY ice. In the Canadian basin, the age of thick, deformed sea ice reaches 4–5 years. The average over ice categories hides the variations of age among ice of different thickness. The age of the thickest ice reaches 10 years in deformed regions.

The simulated NH geographical distribution of sea ice age qualitatively agrees with available observation-based inferences from PMW ice motion and concentration (Rigor and Wallace, 2004; Belchansky et al., 2005b). First, the computed MY ice edge compares well with the 15% MY ice concentration contour of PMW neural network derivations (Belchansky et al., 2005a). Nevertheless, the model seems to underestimate the MY ice area in the Atlantic sector of the Arctic Ocean, i.e., where the model underestimates ice thickness. Second, the magnitude of the simulated maximum (4–6 years) is much smaller than observed. The observed maximum is larger than 10 years, and reaches up to 20 years in some cases. Observation-based inferences only take ice transport into account. In the model, three mechanisms decrease the mean and maximum sea ice age compared with satellite-derived values. First, new ice growth inside the pack adds areas of age zero. Second, ice deformation merges the ages of thin deforming ice (young) with thick deformed ice (old). Finally, the merging of ice between neighbour cells following ice transport diffuses the maxima of ice age. This explains why the observation-based inferences of sea ice age are higher.

The simulated oldest ice is located a few hundreds of kilometers off the Canadian coast. Under off-shore winds, the pack ice drifts

off the coast and some new ice (age 0) is created in the coastal open water. When the wind direction switches back to the South, the new ice is piled up and incorporated into older ridges, reducing the local sea ice age. In observation-derived values, the sea ice maximum is situated in the Beaufort Gyre. More work should be done to attribute the origins of these differences.

Southern Hemisphere. In the SH, the simulated ice age rarely exceeds two years, and averaged over 1979–2006, it does not exceed one year. Typically, the sea ice age equals zero at the ice edge and increases southwards. The ice age shows maxima in the Weddell and Ross Seas, where the ice is on average 6 months old. In the Amundsen and Bellingshausen Seas, the ice is younger (2–3 months). Associated to the aforementioned underestimation of ice thickness in the Weddell, Amundsen, Bellingshausen and Ross Seas, we believe the sea ice age is underestimated. This is corroborated by the observation of second-year or even MY ice in those regions (e.g., Eicken, 1998). The ice is the youngest (0–2 months on average) off East Antarctica. The near zero sea ice age in Western Ross Sea and in several places along East Antarctica reveals the presence of simulated polynyas. There is no large-scale sea ice age dataset in the SH.

Despite the fact that the hemispheric ice age is not well correlated with the total hemispheric volume, the similarity between age and thickness geographical distributions is striking. Point to point correlations between single-category age and thickness averaged over 1979–2006 in the NH (SH) give correlations of 0.69 (0.52). Computed over smaller time periods, the correlation reaches up to 0.8, but the value of the age–thickness regression coefficient changes with season and from year to year. Therefore, it is possible that satellite estimates of ice age could be a proxy for ice thickness, but this requires a deeper analysis.

4.7. Ice salinity

Since the simulated sea ice salinity field is validated and analyzed in detail in the companion paper, we only describe it briefly here. Fig. 15 shows the simulated time series of global hemispheric means of ice salinity. Mean ice salinity is 3.6 (resp. 6.3) ‰ in the NH (SH). The sea ice salinity is higher in the SH because of (1) the higher relative contribution of young ice, (2) the much lower frequency of surface melt and therefore of flushing and (3) the higher contribution of snow ice formation to the global ice mass balance.
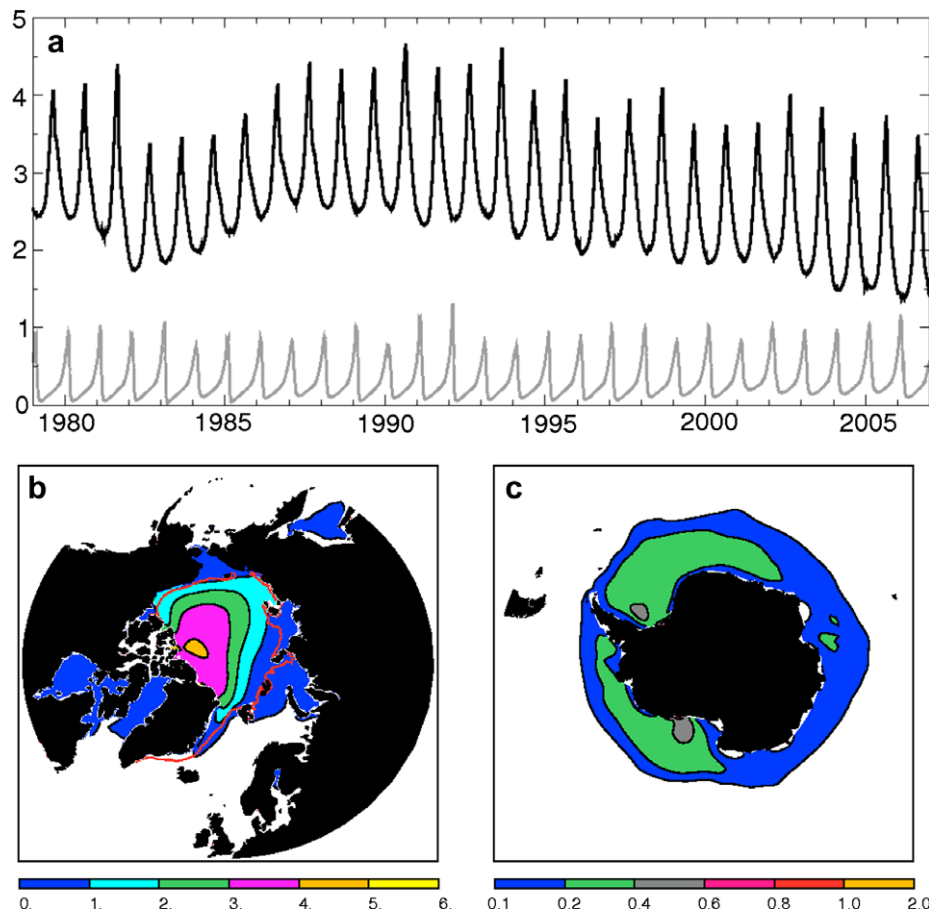
Fig. 14. Sea ice age (years), area-weighed average over all ice thickness categories, excluding open water. (a) Simulated time series of global hemispheric means for the NH (black) and SH (grey). (b and c) Geographical distribution for the NH (March, b, years) and the SH (September, c, years). The observed MY ice edge derived from neural network analysis of passive microwave data (Belchansky et al., 2005a) is drawn in red on (b) panel.

The seasonal cycle of sea ice salinity has an average amplitude of 2‰ in the NH (4.8‰ in the SH), with a maximum in winter (fall) and a minimum in summer (summer). Interannual variability in ice salinity is mostly driven by the maximum value, which reflects the relative contribution of young ice to the total ice volume, itself depending on the amount of summer melt. Salinity and age seem to be highly related to each other, as indicated by the high correlation between the daily mean salinity and age time series of −0.83 (−0.71). The trend in hemispheric mean ice salinity, governed by the trend in the seasonal maximum, is significant only in the NH.

5. Discussion and conclusions

We have presented results from LIM3, a new dynamic–thermodynamic sea ice model, including the representation of subgrid-scale distributions of ice thickness, enthalpy, salinity and age. LIM3 is embedded in the ocean modelling system NEMO in a global configuration.

Despite the fact that the model is global and the parameter values are the same for both hemispheres, the simulated NH and SH sea ice covers are characterized by different physics. In the NH, the simulated sea ice is thicker, older and less saline than in the SH. Ice grows mostly by basal congelation and melts by comparable amounts at the top and bottom interfaces. In the SH, the three different growth mechanisms included in the model (basal congelation, new ice formation in open water and snow ice formation) contribute significantly. This north–south contrast in the sources and sinks of ice mass is quite realistic compared with the information from the textural analysis of ice cores.
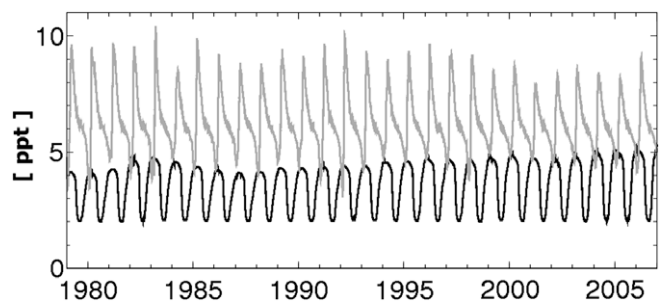

Fig. 15. Simulated time series of hemispheric mean sea ice salinity (volume-weighed average over all categories, excluding open water) for the NH (black) and SH (grey).

In the NH, the model provides a reasonably good simulation of the large-scale sea ice features, in line with the most advanced AOMIP models (Gerdes and Köberle, 2007; Johnson et al., 2007). The mean seasonal cycle of ice extent as well as the mean geographical distribution of ice concentration are rather realistic compared with observations derived from satellite PMW recordings. The geographical distribution of ice thickness and concentration is much better simulated in LIM3 than in earlier versions of LIM due to a more sophisticated ice-albedo feedback associated with the introduction of the ITD in the model. Local model errors are found in the Odden region in winter and in the Atlantic sector of the Arctic Ocean in summer. The 1979–2006 interannual variations of ice coverage are well captured by the model. The simulated ice thickness

generally agrees with ULS observations, though the model overestimates ice thickness in the Beaufort Gyre and underestimates it in the Atlantic sector of the Arctic Ocean, which is presumably due to an misrepresentation of shear effects in the model. The simulated drift is in agreement with PMW inferences of ice motion. The ice areal export through Fram Strait is well simulated. Nevertheless, as a result of the underestimation of ice thickness near the North Pole, the volume export through Fram Strait is underestimated. Information is too limited to draw any conclusion regarding the simulated snow depth in the Arctic.

In the SH, the seasonal variations of ice extent are rather well represented compared with PMW observations. The winter ice extent is well simulated, though the winter ice area and concentrations are overestimated. In summer, the ice retreats too far southward in the model. The simulated geographical distribution of ice thickness resembles the observations, with a tendency towards underestimation, in particular in coastal seas. Compared to PMW observations, snow depth is quite realistic in the model. In addition, the general features of ice drift are well reproduced, though the coastal currents are significantly overestimated by the model. The formation of new ice in open water is underestimated when compared with the granular ice frequency (i.e., ice originating from open water) in ice cores from several Antarctic subregions. The overestimation of winter ice concentration, the yearlong underestimation of ice thickness and the underestimation of new ice growth in open water all suggest that the representation of dynamical (including pancake) processes of ice growth should be improved in the model.

The age of sea ice is a new feature included in the model. The NH FY–MY ice contrast is well simulated. In the SH, the simulated ice age is much smaller than in the Arctic and reflects a younger MY ice cover than in the NH. In the NH, the values and the geographical distribution of sea ice age within the perennial ice zone differ from satellite observation-based inferences. Based on the use of age in marine modelling (Deleersnijder et al., 2001), we argue that this reflects mostly the fact that the definitions of observed and model ice age are different. Nevertheless, this could also indicate model misbehaviour, though this is difficult to disentangle at this stage. Consequently, the simulation of sea ice age deserves an entire study which is beyond the scope of the present paper. Another new feature included into the model is the sea ice salinity. The simulated ice salinities show strong hemispheric and seasonal differences, which reflect the spatio-temporal variations in the thermodynamic regime and will be investigated in detail in the second part of the present paper.

The sea ice model used here, LIM3, has a level of sophistication that warrants a reasonable level of agreement with available observations. The present study however confirms that sea ice models are still far from perfect. LIM3, for instance, significantly underestimates ice thickness in both hemispheres. There are various problematic features in the model (e.g., grid resolution, representation of strain rates, no melt ponds or pancake cycle, crude representation of snow, redistribution scheme, heat input from the ocean), as well as serious uncertainties in the forcing. It is not yet clear, though, what are the major causes of model uncertainty and more work has to be done to understand and address those problems. Nevertheless, within the scope of present knowledge and uncertainties, LIM3 is certainly suitable for large-scale sea ice and climate simulations.

Acknowledgements

References

Aagaard, K.A., Carmack, E.C., 1989. The role of sea ice and other fresh water in the Arctic circulation. Journal of Geophysical Research 94, 14485–14498 .

Ackley, S.F., Sullivan, C.W., 1994. Physical controls on the development and characteristics of Antarctic sea ice biological communities – a review and synthesis. Deep-Sea Research 41, 1583–1600.

Andreas, E.L., Ackley, S.F., 1982. On the differences in ablation seasons of the Arctic and Antarctic sea ice. Journal of Atmospheric Sciences 39, 440–447.

Arzel, O., Fichefet, T., Goosse, H., 2006. Sea ice evolution over the 20th and 21st centuries as simulated by current AOGCMs. Ocean Modelling 12, 401–415.

Babko, O., Rothrock, D.A., Maykut, G.A., 2002. Role of rafting in the mechanical redistribution of sea ice thickness. Journal of Geophysical Research, 107. doi:10.1029/1999JC000190.

Barnier, B., Madec, G., Penduff, T., Molines, J.-M., Tréguier, A.-M., Le Sommer, J., Beckmann, A., Biastoch, A., Bing, C., Dengg, J., Derval, C., Durand, E., Gulev, S., Ry, E., Talandier, C., Theetten, S., Maltrud, M.E., McClean, J., De Cuevas, B., 2006. Impact of partial steps and momentum advection schemes in a global ocean circulation model at eddy-permitting resolution. Ocean Dynamics, doi:10.1007/s10236-006-0082-1.

Baumgartner, F., Reichel, E., 1975. The World Water Balance: Mean Annual Global, Continental and Maritime Precipitation, Evaporation and Runoff. Elsevier, Amsterdam (p. 179).

Belchansky, G.I., Douglas, D.C., Eremeev, V.A., Platonov, N.G., 2005a. Variations in the Arctic's multiyear sea ice cover: A neural network analysis of SMMR–SSM/I data, 1979–2004. Geophysical Research Letters 32, L09605. doi:10.1029/2005GL022395.

Belchansky, G.I., Douglas, D.C., Platonov, N.G., 2005b. Spatial and temporal variations in the age structure of Arctic sea ice. Geophysical Research Letters 32, L18504. doi:10.1029/2005GL023976.

Berliand, M.E., Strokina, T.G., 1980. Global distribution of the total amount of clouds. Hydrometeorological, Leningrad, 71 (in Russian).

Biggs, N.R.T., Morales Maqueda, M.A., Willmott, A.J., 2000. Polynya flux model solutions incorporating a parameterization for the collection thickness of consolidated new ice. Journal of Fluid Mechanics 408, 179–204.

Bitz, C.M., Lipscomb, W.H., 1999. An energy-conserving thermodynamic model of sea ice. Journal of Geophysical Research 104, 15669–15677.

Bitz, C.M., Holland, M.M., Weaver, A.J., Eby, M., 2001. Simulating the ice-thickness distribution in a coupled climate model. Journal of Geophysical Research 106, 2441–2463.

Blanke, B., Delecluse, P., 1993. Variability of the tropical Atlantic ocean simulated by a general circulation model with two different mixed layer physics. Journal of Physical Oceanography 23, 1363–1388.

Bouillon, S., Morales Maqueda, M.A., Fichefet, T., Legat, V., 2009. An Elastic–Viscous–Plastic Sea Ice Model formulated on Arakawa B and C grids. Ocean Modelling.

Brandt, R.E., Warren, S.G., Worby, A.P., Grenfell, T.C., 2005. Surface albedo of the Antarctic sea ice zone. Journal of Climate 18, 3606–3622.

Cavalieri, D.J., Gloersen, P., Parkinson, C.L., Comiso, J.C., Zwally, H.J., 1997. Observed hemispheric asymmetry in global sea ice changes. Science 272, 1104–1106.

Cavalieri, D.J., Parkinson, C.L., Vinnikov, K.Y., 2003. 30-Year satellite record reveals contrasting Arctic and Antarctic sea ice variability. Geophysical Research Letters 30 (18), 1970. doi:10.1029/2003GL018031.

Comiso, J.C., 2007. Bootstrap sea ice concentrations from NIMBUS-7 SMMR and DMSP SSM/I, 1979–2006. Boulder, Colorado USA: National Snow and Ice Data Center. Digital Media.

Comiso, J.C., 2006. Abrupt decline in the Arctic winter sea ice cover. Geophysical Research Letters 33, L18504. doi:10.1029/2006GL027341.

Comiso, J.C., Nishio, F., 2008. Trends in the sea ice cover using enhanced and compatible AMSR-E, SSM/I, and SMMR data. Journal of Geophysical Research 113, C02S07. doi:10.1029/2007JC004257.

Comiso, J.C., Parkinson, C.L., Gersten, R., Stock, L., 2008. Accelerated decline in the Arctic sea ice cover. Geophysical Research Letters 35, L01703. doi:10.1029/2007GL031972.

Comiso, J.C., Wadhams, P., Pedersen, L.T., Gersten, R.A., 2001. Seasonal and interannual variability of the Odden ice tongue and a study of environmental effects. Journal of Geophysical Research 106 (C5), 9093–9116.

Cox, G.F.N., Weeks, W.F., 1975. Brine drainage and initial salt entrapment in sodium chloride ice. CRREL Report 345, 85. U.S. Army Cold Reg. Res. and Eng. Lab., Hanover, N.H.

Cox, G.F.N., Weeks, W.F., 1988. Numerical simulations of the profile properties of undeformed first-year sea ice during growth season. Journal of Geophysical Research 93, 12449–12460.

Deleersnijder, E., Campin, J.-M., Delhez, E.J.M., 2001. The concept of age in marine modelling: I. Theory and preliminary model results. Journal of Marine Systems 28, 229–267.

Delille, B., 2006. Inorganic carbon dynamics and air–ice–sea CO_2 fluxes in the open and coastal waters of the Southern Ocean. Ph.d. Thesis, Université de Liège.

Déry, S.J., Tremblay, L.-B., 2004. Modeling the effects of wind redistribution on the snow mass budget of polar sea ice. Journal of Physical Oceanography 34 (1), 258–271.

Ebert, E.E., Curry, J.A., 1993. An intermediate one-dimensional thermodynamic sea ice model for investigating ice–atmosphere interactions. Journal of Geophysical Research 98, 10085–10109.

Eicken, H., 1998. Factors determining microstructure, salinity and stable isotope composition of Antarctic sea ice: deriving modes and rates of ice growth in the Weddell Sea. In: Jeffries, M.O. (Ed.), Antarctic Sea Ice: Physical Processes, Interactions and Variability, Antarctic Research Series, 74, 89–122, AGU, Washington, DC.

Fedotov, V.I., Cherepanov, N.V., Tyshko, K.P., 1998. Some features of the growth, structure and metamorphism of East Antarctic sea ice. In: Jeffries, M.O. (Ed.), Antarctic Sea Ice: Physical Processes, Interactions and Variability, Antarctic Research Series, 74, AGU, Washington, DC, 89–122.

Fichefet, T., Morales Maqueda, M.A., 1997. Sensitivity of a global sea ice model to the treatment of ice thermodynamics and dynamics. Journal of Geophysical Research 102, 12609–12646.

Fichefet, T., Tartinville, B., Goosse, H., 2000. Sensitivity of the Antarctic sea ice to the thermal conductivity of snow. Geophysical Research Letters 27, 401–404.

Flato, G.M., Hibler, W.D., 1995. Ridging and strength in modeling the thickness distribution of Arctic sea ice. Journal of Geophysical Research 100, 18611–18626.

Fowler, C., 2003. Polar Pathfinder Daily 25 km EASE-GRID Sea Ice Motion Vectors. Boulder, CO, USA: National Snow and Ice Data Center. Digital Media.

Fritsen, C., Ackley, S.F., Kremer, J.N., Sullivan, C.W., 1998. Flood–freeze cycles and microalgal dynamics in Antarctic pack ice. In: Lizotte, M.P., Arrigo, K. (Eds.), Antarctic Sea Ice: Biological Processes, Interactions, and Variability, Antarctic Research Series, 73. AGU, Washington, DC.

Gent, P.R., McWilliams, J.C., 1990. Isopycnal mixing in ocean circulation models. Journal of Physical Oceanography 20, 150–155.

Gerdes, R., Köberle, C., 2007. Comparison of Arctic sea ice thickness variability in IPCC climate of the 20th century experiments and in ocean–sea ice hindcasts. Journal of Geophysical Research 112 (C4), C04S13. doi:10.1029/2006JC003616.

Goodison, B.E., Louie, P.Y.T., Yang, D., 1998. WMO Solid precipitation measurement intercomparison final report. WMO Instruments and Observing Methods Report, 67, WMO/TD No. 872.

Goosse, H., 1997. Modelling the large-scale behaviour of the coupled ocean–sea–ice system. Ph.d. Thesis, Université catholique de Louvain, Louvain- la-Neuve, Belgium.

Goosse, H., Fichefet, T., 1999. Importance of ice–ocean interactions for the global ocean circulation: a model study. Journal of Geophysical Research 104, 23337–23355.

Haapala, J., 2000. On the modeling of ice thickness redistribution. Journal of Glaciology 46 (154), 427–437.

Haas, C., 2004. Late-summer sea ice thickness variability in the Arctic Transpolar Drift 1991–2001 derived from ground-based electromagnetic sounding. Geophysical Research Letters 31, L09402. doi:10.1029/2003GL019394.

Haas, C., Thomas, D.N., Bareiss, J., 2001. Surface properties and processes of perennial Antarctic sea ice in summer. Journal of Glaciology 47, 613–625.

Harder, M., Lemke, P., 1994. Modelling the extent of sea ice ridging in the weddell sea. In: Johannessen, O.M., Muench, R.D., Overland, J.E. (Ed.), The Polar Oceans and Their Role in Shaping the Global Environment, Geophysical Monograph, 85, 187–197.

Hibler III, W.D., 1979. A dynamic–thermodynamic sea ice model. Journal of Physical Oceanography 9, 815–846.

Hibler III, W.D., 1980. Modeling a variable thickness sea ice cover. Monthly Weather Review 108, 1943–1973.

Holland, M.M., Bitz, C.M., Hunke, E.C., Lipscomb, W.H., Schramm, J., 2006. Influence of the sea ice thickness distribution on polar climate in CCSM3. Journal of Climate 19, 2398–2414.

Høyland, K.V., 2002. Consolidation of first-year sea ice ridges. Journal of Geophysical Research 107 (C6), 3062. doi:10.1029/2000JC000526.

Hunke, E.C., 2001. Viscous plastic sea ice dynamics with the EVP model: linearization issues. Journal of Computational Physics 170, 18–38. doi:10.1006/jcph.2001.6710.

Hunke, E.C., Dukowicz, J.K., 1997. An elastic–viscous–plastic model for sea ice dynamics. Journal of Physical Oceanography 27, 1849–1867.

Hunke, E.C., Holland, M.M., 2007. Global atmospheric forcing data for Arctic ice–ocean modeling. Journal of Geophysical Research 12, C04S14. doi:10.1029/2006JC003640.

Hunke, E.C., Lipscomb, W.H., 2004. CICE: The Los Alamos Sea Ice Model, documentation and software user's manual, version 3. LACC-98-16, Los Alamos National Laboratory, Los Alamos, New Mexico.

Hunke, E.C., Zhang, Y., 1999. A comparison of sea ice dynamics models at high resolution. Monthly Weather Review 127, 396–408.

Jackett, D.R., McDougall, T.J., 1995. Minimal adjustment of hydrographic profiles to achieve static stability. Journal of Atmospheric and Oceanic Technology 12 (2), 381–389.

Jeffries, M.O., Worby, A.P., Morris, K., Weeks, W.F., 1997. Seasonal variations in the properties and structural composition of sea ice and snow cover in the Bellingshausen and Amundsen Sea, Antarctica. Journal of Glaciology 43 (143), 138–151.

Johnson, M., Gaffigan, S., Hunke, E., Gerdes, R., 2007. A comparison of Arctic Ocean sea ice concentration among the coordinated AOMIP model experiments. Journal of Geophysical Research 112, C04S11. doi:10.1029/2006JC003690.

Kalnay, E., Kanamitsu, M., Kistler, R., Collins, W., Deaven, D., Gandin, L., Iredell, M., Saha, S., White, G., Woollen, J., Zhu, Y., Leetmaa, A., Reynolds, B., Chelliah, M., Ebisuzaki, W., Higgins, W., Janowiak, J., Mo, K., Ropelewski, C., Wang, J., Jenne, R., Joseph, D., 1996. The NCEP/NCAR 40-year reanalysis project. Bulletin of the American Meteorological Society 77, 437–471.

Kovacs, A., 1996. Sea ice, part I, bulk salinity versus ice floe thickness. CRREL Report, 96-7, 16 pp., U.S. Army Cold Reg. Res. and Eng. Lab., Hanover, N.H.

Kwok, R., 2002. Sea ice concentration estimates from satellite passive microwave radiometry and openings from SAR ice motion. Geophysical Research Letters 29 (9). doi: 1311.10.1029/2002GL014787.

Kwok, R., 2004. Annual cycles of multiyear sea ice coverage of the Arctic Ocean: 1999–2003. Journal of Geophysical Research 109, C11004. doi:10.1029/2003JC002238.

Kwok, R., Cunningham, G.F., Pang, S.S., 2004. Fram Strait sea ice outflow. Journal of Geophysical Research 109, C01009. doi:10.1029/2003JC001785.

Kwok, R., Cunningham, G.F., 2008. ICESat over Arctic sea ice: estimation of snow depth and ice thickness. Journal of Geophysical Research 113, C08010. doi:10.1029/2008JC004753.

Lange, M.A., Ackley, S.F., Wadhams, P., Dieckmann, G.S., Eicken, H., 1989. Development of sea ice in the Weddell Sea. Annals of Glaciology 12, 92–96.

Lange, M.A., Eicken, H., 1991. The sea ice thickness distribution in the Northwestern Weddell Sea. Journal of Geophysical Research 96, 4821–4837.

Large, W.G., Yeager, S.G., 2004. Diurnal to decadal global forcing for ocean and sea ice models: the datasets and climatologies. NCAR Technical Report, TN-460+STR, p. 105.

Lannuzel, D., Schoemann, V., de Jong, J., Tison, J., Chou, L., 2007. Distribution and biogeochemical behaviour of iron in the East Antarctic sea ice. Marine Chemistry 106 (1–2), 18–32. doi:10.1016/j.marchem.2006.06.010.

Laxon, S., Peacock, N., Smith, D., 2003. High interannual variability of sea ice thickness in the Arctic region. Nature 425, 947–950. doi:10.1038/nature02050.

Lefebvre, W., Goosse, H., 2008. Analysis of the projected regional sea ice changes in the Southern Ocean during the 21st century. Climate Dynamics 30, 59–76. doi:10.1007/s00382-007-0273-6.

Leppäranta, M., Lensu, M., Koslof, P., Witch, B., 1995. The life story of a first-year sea ice ridge. Cold Regions Science and Technology 23 (3), 279–290.

Lindsay, R.W., Zhang, J., 2005. The thinning of arctic sea ice, 1988–2003: have we passed a tipping point? Journal of Climate 18, 4879–4894.

Lipscomb, W.H., 2001. Remapping the thickness distribution in sea ice models. Journal of Geophysical Research 106 (C7), 13989–14000.

Lipscomb, W.H., Hunke, E.C., Maslowski, W., Jakacki, J., 2007. Ridging, strength, and stability in high-resolution sea ice models. Journal of Geophysical Research 112, C03S91. doi:10.1029/2005JC003355.

Lytle, V., Ackley, S., 1996. Heat flux through sea ice in the Western Weddell Sea: convective and conductive transfer processes. Journal of Geophysical Research 101 (C4), 8853–8868.

Madec, G., 2008. NEMO reference manual, ocean dynamics component: NEMO–OPA. Note du Pole de modélisation, Institut Pierre-Simon Laplace (IPSL), France, No. 27 ISSN No. 1288-1619. Available from: <http://www.lodyc.jussieu.fr/NEMO/general/manual/NEMO_book.pdf>.

Malmgren, F., 1927. On the properties of sea ice. In: Sverdrup, H.U. (Ed.), The Norwegian North Polar Expedition with the 'Maud' 1918–1925, vol. 1a(5). John Griegds Boktr., Bergen, Norway.

Markus, T., Cavalieri, D.J., 1998. Snow depth distribution over sea ice in the Southern Ocean from satellite passive microwave data. In: Jeffries, M.O. (Ed.), Antarctic Sea Ice: Physical Processes, Interactions and Variability, Antarctic Research Series. AGU, Washington, DC, pp. 19–39.

Markus, T., Cavalieri, D.J., 2006. Interannual and regional variability of Southern Ocean snow on sea ice and its correspondence with sea ice cover and atmospheric circulation patterns. Annals of Glaciology 46, 53–57.

Massom, R.A. et al., 2001. Snow on Antarctic sea ice. Review of Geophysics 39 (3), 413–445.

Maykut, G.A., 1986. The surface heat and mass balance. In: Untersteiner, N. (Ed.), The Geophysics of Sea Ice. NATO ASI Series B: Physics, vol. 146. Plenum Press, New York, pp. 395–464.

Maykut, G.A., Untersteiner, N., 1971. Some results from a time-dependent thermodynamic model of sea ice. Journal of Geophysical Research 76, 1550–1575.

McPhee, M.G., 1992. Turbulent heat flux in the upper ocean under sea ice. Journal of Geophysical Research 97 (C4), 5365–5379.

McPhee, M.G., Kottmeier, C., Morison, J.H., 1998. Ocean heat flux in the Central Weddell Sea during winter. Journal of Physical Oceanography 29, 1166–1179.

Nicolaus, M., Haas, C., Bareiss, J., Willmes, S., 2006. A model study of differences of snow thinning on Arctic and Antarctic first-year sea ice during spring and summer. Annals of Glaciology 44, 147–153.

Oberhuber, J.M., 1993. Simulation of the Atlantic circulation with a coupled sea ice-mixed layer-isopycnal general circulation model. Part I: model description. Journal of Physical Oceanography 23, 808–829.

Pacanowski, R.C., Gnanadesikan, A., 1998. Transient response in a Z-level ocean model that resolves topography with partial cells. Monthly Weather Review 126 (12), 3248–3270.

Parmerter, R.R., 1975. A model of simple rafting in sea ice. Journal of Geophysical Research 80, 1948–1952.

Perovich, D.K., Grenfell, T.C., Light, B., Hobbs, P.V., 2002. Seasonal evolution of the albedo of multiyear Arctic sea ice. Journal of Geophysical Research 107 (C10), 8044. doi:10.1029/2000JC000438.

Perovich, D.K., Grenfell, T.C., Richter-Menge, J.A., Light, B., Tucker III, W.B., Eicken, H., 2003. Thin and thinner: Sea ice mass balance measurements during SHEBA. Journal of Geophysical Research 108 (C3), 8050. doi:10.1029/2001JC001079, 2003.

Prather, M., 1986. Numerical advection by conservation of second-order moments. Journal of Geophysical Research 91, 6671–6681.

Pringle, D.J., Eicken, H., Trodahl, H.J., Backstrom, L.G.E., 2007. Thermal conductivity of landfast Antarctic and Arctic sea ice. Journal of Geophysical Research 112, C04017. doi:10.1029/2006JC003641.

Rigor, I.G., Wallace, J.M., 2004. Variations in the age of sea ice and summer sea ice extent. Geophysical Research Letters, 31. doi:10.1029/2004GL019492.

Rigor, I.G., Wallace, J.M., Colony, R.I., 2002. On the response of sea ice to the Arctic Oscillation. Journal of Climate 15, 2648–2668.

Rothrock, D.A., Percival, D.B., Wensnahan, M., 2003. The decline in arctic sea–ice thickness: separating the spatial, annual, and interannual variability in a quarter century of submarine data. Journal of Geophysical Research 113, C05003. doi:10.1029/2007JC004252.

Rothrock, D.A., Zhang, J., Yu, Y., 2003. The arctic ice thickness anomaly of the 1990s: a consistent view from observations and models. Journal of Geophysical Research 108 (C3), 3083. doi:10.1029/2001JC001208.

Shine, K.P., Henderson-Sellers, A., 1985. The sensitivity of a thermodynamic sea ice model to changes in surface albedo parameterization. Journal of Geophysical Research 90, 2243–2250.

Semtner Jr., A.J., 1976. A model for the thermodynamic growth of sea ice in numerical investigations of climate. Journal of Physical Oceanography 6, 379–389.

Serreze, M.C., Holland, M.M., Stroeve, J., 2007. Perspectives on the Arctic's shrinking sea–ice cover. Science 315, 1533–1536. doi:10.1126/science.1139426.

Steele, M., 1992. Sea ice melting and floe geometry in a simple ice–ocean model. Journal of Geophysical Research 97 (C11), 17729–17738.

Steele, M., Morfley, R., Ermold, W., 2001. PHC: a global ocean hydrography with a high-quality Arctic Ocean. Journal of Climate 14, 2079–2087.

Stroeve, J.C., Serreze, M.C., Fetterer, F., Arbetter, T., Meier, W., Maslanik, J., Knowles, K., 2005. Tracking the Arctic's shrinking ice cover: another extreme September minimum in 2004. Geophysical Research Letters 32, L04501. doi:10.1029/2004GL021810.

Stroeve, J., Holland, M.M., Meier, W., Scambos, T., Serreze, M., 2007. Arctic sea ice decline: faster than forecast. Geophysical Research Letters 34, L09501. doi:10.1029/2007GL029703.

Sturm, M., Perovich, D.K., Holmgren, J., 2002. Thermal conductivity and heat transfer through the snow on the ice of the Beaufort Sea. Journal of Geophysical Research 107 (C10), 8043. doi:10.1029/2000JC000409.

Tartinville, B., Campin, J.M., Fichefet, T., Goosse, H., 2001. Realistic representation of the surface freshwater flux in an ice–ocean general circulation model. Ocean Modelling 3 (1–2), 95–108.

Thorndike, A.S., Rothrock, D.A., Maykut, G.A., Colony, R., 1975. The thickness distribution of sea ice. Journal of Geophysical Research 80, 4501–4513.

Timmermann, R., Goosse, H., Madec, G., Fichefet, T., Ethe, C., Dulière, V., 2005. On the representation of high latitude processes in the ORCALIM global coupled sea ice–ocean model. Ocean Modelling 8, 175–201.

Tremblay, L.-B., Hakakian, M., 2006. Estimating the sea–ice compressive strength from satellite-derived sea–ice drift and NCEP reanalysis data. Journal of Physical Oceanography 36, 2165–2172.

Trenberth, K.E., Olson, J.G., Large, W.G., 1989. A Global Ocean Wind Stress Climatology Based on the ECMWF Analyses. National Center for Atmospheric Research, Boulder, Colorado, NCAR/TN-338+STR, p. 93.

Tucker III, W.B., Gow, A.J., Weeks, W.F., 1987. Physical properties of summer sea ice in the Fram Strait. Journal of Geophysical Research 92, 6787–6803.

Tuhkuri, J., Lensu, M., 2002. Laboratory tests on ridging and rafting of ice sheets. Journal of Geophysical Research 107 (C9), 3125. doi:10.1029/2001JC000848.

Untersteiner, N., 1968. Natural desalination and equilibrium salinity profile of perennial sea ice. Journal of Geophysical Research 73, 1251–1257.

Vancoppenolle, M., Bitz, C.M., Fichefet, T., 2007. Summer landfast sea ice desalination at Point Barrow, Alaska: model and observations. Journal of Geophysical Research 112, C04022. doi:10.1029/2006JC003493.

Vancoppenolle, M., Fichefet, T., Bitz, C.M., 2005. On the sensitivity of undeformed Arctic sea ice to its vertical salinity profile. Geophysical Research Letters 32, L16502. doi:10.1029/2005GL023427.

Vancoppenolle, M., Fichefet, T., Bitz, C.M., 2006. Modeling the salinity profile of undeformed Arctic sea ice. Geophysical Research Letters 33, L21501. doi:10.1029/2006GL028342.

Vancoppenolle, M., 2008. Modelling the mass balance and salinity of Arctic and Antarctic sea ice. Ph.d. Thesis, Université catholique de Louvain, ISBN 978-2-87463-113-9. Available from: <http://edoc.bib.ucl.ac.be:81/ETD-db/collection/available/BelnUcetd-02252008-180131/>.

Vancoppenolle, M., Fichefet, T., Goosse, H., 2009. Simulating the mass balance and salinity of Arctic and Antarctic sea ice. 2. Importance of salinity variations. Ocean Modelling 27 (1–2), 54–69.

Warren, S.G., Rigor, I.G., Untersteiner, N., Radionov, V.F., Bryazgin, N.N., Aleksandrov, Y.I., Colony, R., 1999. Snow depth on Arctic sea ice. Journal of Climate 12, 1814–1829.

Widell, K., Fer., I., Haugan, P.M., 2006. Salt release from warming sea ice. Geophys. Res. Lett. 33, L12501.

Wilchinsky, A.V., Feltham, D.L., Miller, P.A., 2006. A multi-thickness sea ice model accounting for sliding friction. Journal of Physical Oceanography 36, 1719–1738.

Witte, H., Fahrbach, E., 2005. AWI Moored ULS Data, Greenland Sea and Fram Strait, 1991–2002. Boulder, CO: National Snow and Ice Data Center/World Data Center for Glaciology. Digital Media.

Worby, A.P., Jeffries, M.O., Weeks, W.F., Morris, K., Jaña, R., 1996. The thickness distribution of sea ice and snow cover during late winter in the Bellingshausen and Amundsen Seas, Antarctica. Journal of Geophysical Research 101 (C12), 28441–28455.

Worby, A.P., Massom, R.A., Allison, I., Lytle, V.I., Heil, P., 1998. East Antarctic sea ice: a review of its structure, properties and drift, In: Jeffries, M.O. (Ed.), Antarctic Sea Ice: Physical Processes, Interactions and Variability, Antarctic Research Series, 74, AGU, Washington, DC, pp. 89–122.

Worby, A.P., Geiger, C.A., Paget, M.J., Van Woert, M.L., Ackley, S.F., DeLiberty, T.L., 2008. The thickness distribution of Antarctic sea ice. Journal of Geophysical Research 113, C05S92. doi:10.1029/2007JC004254.

Zhang, J., Hibler III, W.D., 1997. On an efficient numerical method for modeling sea ice dynamics. Journal of Geophysical Research 102 (C4), 8691–8702.

Zhang, J., Rothrock, D.A., 2003. Modeling global sea ice with a thickness and enthalpy distribution model in generalized curvilinear coordinates. Monthly Weather Review 131, 845–861.

Zhang, X., Walsh, J.E., 2006. Toward a seasonally ice-covered arctic ocean: scenarios from the IPCC AR4 model simulations. Journal of Climate 19, 1730–1747.

Zwally, H.J., Yi, D., Kwok, R., Zhao, Y., 2008. ICESat measurements of sea ice freeboard and estimates of sea ice thickness in the Weddell Sea. Journal of Geophysical Research 113, C02S15. doi:10.1029/2007JC004284.